Vadose Zone Journal
ORIGINAL RESEARCH

Modeling the Water and Energy Balance of Vegetated Areas with Snow Accumulation

T. J. Kelleners,* D. G. Chandler, J. P. McNamara, M. M. Gribb, and M. S. Seyfried

The ability to quantify soil–atmosphere water and energy exchange is important in understanding agricultural and natural ecosystems, as well as the earth's climate. We developed a one-dimensional vertical model that calculates solar radiation, canopy energy balance, surface energy balance, snowpack dynamics, soil water flow, and snow–soil–bedrock heat exchange, including soil water freezing. The processes are loosely coupled (solved sequentially) to limit the computational burden. The model was applied to describe water and energy dynamics for a northeast-facing mountain slope in the Dry Creek Experimental Watershed near Boise, ID. Calibration was achieved by optimizing the saturated soil hydraulic conductivity. Validation results showed that the model can successfully calculate seasonal dynamics in snow height, soil water content, and soil temperature. Both the calibration and validation years confirmed earlier results that evapotranspiration on the northeast-facing slope consumes approximately 60% of yearly precipitation, while deep percolation from the soil profile constitutes about 40% of yearly precipitation.

WATER AND ENERGY FLUXES in the soil–plant–atmosphere system are important at the local, regional, and global scales. Direct measurement of these fluxes is generally limited to a few locations and to relatively short periods. Many computer simulation models have been developed to study the spatial and temporal patterns in water and energy fluxes. The models facilitate studying larger spatial domains and longer time periods than would be practical using measurements alone. These models are used in agricultural, ecosystem, and climate research (e.g., Flerchinger et al., 1998; van Dam et al., 2008; Oleson et al., 2008). The number of incorporated processes as well as process detail varies considerably among existing models. This is not surprising given the complex nature of soil–plant–atmosphere water and energy fluxes, which results in many interacting factors.

T.J. Kelleners, Renewable Resources Dep., Univ. of Wyoming, Laramie, WY 82071; D.G. Chandler, Dep. of Civil Engineering, Kansas State Univ., Manhattan, KS 66506; J.P. McNamara, Dep. of Geosciences, Boise State Univ., Boise, ID 83725; M.M. Gribb, Dep. of Civil Engineering, Boise State Univ., Boise, ID 83725; and M.S. Seyfried, USDA-ARS, Northwest Watershed Research Center, Boise, ID 83712. *Corresponding author (tkellene@uwyo.edu).

Vadose Zone J. 8:1013–1030
doi:10.2136/vzj2008.0183
Received 23 Dec. 2008.
Published online 13 Sept. 2009.

Modeling of water and energy fluxes in snow-dominated mountainous terrain is particularly challenging. The presence of snow modifies the land surface energy balance considerably. Fresh new snow in particular has a high albedo and a low thermal conductivity, which limits daytime soil warming and nighttime soil cooling. Snow is a complicated medium due to continuously changing properties such as grain size, density, and height. Snow modeling concepts vary from relatively simple single-layer representations (e.g., UEB, Tarboton and Luce, 1996; COUP, Jansson and Karlberg, 2004), to more advanced two-layer representations (e.g., Marks et al., 1998; Koivusalo et al., 2001), to sophisticated multilayer numerical approaches (Anderson, 1976; SNTHERM, Jordan, 1991; Lehning et al., 2006).

Soil freeze–thaw may have an important impact on the water and energy fluxes in mountainous terrain. This is especially true during periods in which the snow cover is limited so that the soil is exposed to the atmosphere. Freezing of soil water produces heat, keeping the soil close to 0°C. In contrast, the melting of soil ice requires energy, which delays soil warm-up during spring. Most current soil freeze–thaw algorithms are based on the Clausius–Clapeyron equation, which is used to relate the freezing point of soil water to soil water potential (Fuchs et al., 1978; Spaans and Baker, 1996; Koren et al., 1999; Niu and Yang, 2006).

Snow can be included in vadose zone models using simple degree day concepts (e.g., HYDRUS, Simunek et al., 2005). More physically based methods for modeling snow accumulation involve calculating the surface energy balance. The most sophisticated approaches calculate both the canopy energy balance and the ground surface energy balance (e.g., SHAW, Flerchinger,

2000; CLM, Oleson et al., 2004). This is accomplished by solving both for leaf temperature and for ground surface temperature. The SHAW model uses relatively simple all-wave expressions to calculate direct and diffuse incoming solar radiation. This all-wave or broadband approach ignores the fact that the albedos of leaves, snow, and soil are all wavelength dependent (Wiscombe and Warren, 1980; Sellers, 1985; Bonan, 1996). The effect of wavelength on the canopy and surface energy balances is included in CLM. This model, however, requires coupling to a global circulation model to obtain accurate estimates of the incoming solar radiation.

We have developed a new model for studying the water and energy balance of mountainous areas that are subject to snow accumulation and melt. A detailed parameterization of the energy fluxes in the soil–plant–atmosphere system was adopted to maximize the model's ability to accurately describe the timing of snowmelt. This was achieved by combining the detailed solar spectrum model of Bird and Riordan (1986) with comprehensive canopy and surface energy balance calculations taken primarily from CLM. To our knowledge, the Bird–Riordan model has not been used before for vadose zone modeling. The single-cloud model of Munro and Young (1982) was used to describe the effect of clouds on the solar radiation. The effect of complex terrain (slope and aspect) on the incoming solar radiation is also incorporated.

Snow in the model is described using a multilayer approach to account for the often nonlinear temperature distribution in this medium. The treatment of bedrock, soil, and snow as a continuum in the vertical heat transport calculation is novel compared with existing vadose zone and land surface models, which generally do not specifically account for the presence of bedrock. The incorporation of bedrock is important in mountainous areas because of the generally shallow soils combined with the moderating effect of bedrock heat storage on soil temperature fluctuations. The model solution strategy, whereby governing equations are loosely coupled rather than tightly coupled, is similar to the solution strategy used in CLM.

The specific objectives of this study were: (i) to develop a computer simulation model that describes the vertical water and energy fluxes between the soil and the atmosphere in snow-dominated, vegetated areas in a detailed yet computationally efficient way; and (ii) to apply the model to a mountain slope to study the effect of snow accumulation on the annual water and energy balance. The motivation for this study was to develop and test an algorithm that could be applied in a spatially distributed way to quantify runoff generation in small, snow-dominated, mountainous catchments. The distributed model application will be a future topic.

Theory

A vertical one-dimensional model was developed to describe the water and energy balance of vegetated areas subject to snow accumulation and melt. Incoming shortwave radiation is estimated using the solar spectral model of Bird and Riordan (1986). Separate energy balance calculations are conducted for the canopy and the ground surface, following the approach used in CLM (Oleson et al., 2004). Snow water flow and storage is calculated assuming gravity flow only. Vertical soil water flow and storage is based on a noniterative solution of Richards' equation following Ross (2003). Vertical heat flux and storage in the snow–soil–bedrock is based on the general heat transport equation. Snow and soil water phase change (between liquid water and ice) is determined separately from the water flow and heat transport calculations. Time stepping in the model is on the order of 15 min except for the soil water flow calculation, which may use smaller time steps. The governing equations are described below.

Precipitation

Meteorological input data include precipitation, relative humidity, air temperature, wind speed, and (calculated) cloud cover. Precipitation p is partitioned into rain and snow using air temperature T_a:

$$p_{sn} = p \qquad T_a \le T_{min} \qquad [1a]$$

$$p_{sn} = \frac{T_{max} - T_a}{T_{max} - T_{min}} p \qquad T_{min} < T_a < T_{max} \qquad [1b]$$

$$p_{sn} = 0 \qquad T_a \ge T_{max} \qquad [1c]$$

with

$$p_r = p - p_{sn} \qquad [1d]$$

where p_r and p_{sn} are the rain and snow rates, respectively. Typical values for the minimum and maximum threshold air temperatures are T_{min} = –1°C and T_{max} = 3°C (U.S. Army Corps of Engineers, 1956). A list of symbols used here is given in Appendix C.

Incoming Shortwave and Longwave Radiation

Incoming shortwave (solar) radiation is calculated in four steps. First, clear-sky (no clouds) direct and diffuse solar radiation is determined using the spectral algorithm of Bird and Riordan (1986). Second, a single-layer cloud model is used to incorporate the effect of clouds (e.g., Munro and Young, 1982). Third, Hay's model is used to calculate slope irradiance (Muneer, 1997). Finally, the spectral estimates of direct and diffuse solar radiation are summed for the visible (<0.7 μm) and near-infrared (≥0.7 μm) wavebands. The distinction between direct and diffuse light is important for assessing the effect of terrain slope and aspect on the energy balance. Visible and near-infrared solar radiation is treated separately because of the associated differences in surface albedo.

Clear-sky direct irradiance on a ground surface normal to the direction of the sun I_{dir0n} for wavelength λ is given by (Bird and Riordan, 1986)

$$I_{dir0n}(\lambda) = I_0(\lambda) d_{es} \tau_o(\lambda) \tau_w(\lambda) \tau_m(\lambda) \tau_R(\lambda) \tau_a(\lambda) \qquad [2]$$

where I_0 is the extraterrestrial irradiance at the mean earth–sun distance for wavelength λ, d_{es} is the dimensionless correction factor for the earth–sun distance, and τ is the dimensionless transmittance of the atmosphere. The subscripts *o*, *w*, *m*, *R*, and *a* denote ozone absorption, water vapor absorption, uniformly mixed gas absorption, molecular Rayleigh scattering, and aerosol attenuation, respectively. Clear-sky diffuse irradiance on a horizontal surface consists of a Rayleigh scattering component I_R, an

aerosol scattering component I_a, and a component that accounts for multiple reflection between the ground and the air I_g (Bird and Riordan, 1986):

$$I_R(\lambda) = I_0(\lambda) d_{es} \cos(\theta) \tau_o(\lambda) \tau_w(\lambda) \tau_m(\lambda) \tau_{aa}(\lambda) \left[1 - \tau_R^{0.95}(\lambda)\right] 0.5 \quad [3a]$$

$$I_a(\lambda) = I_0(\lambda) d_{es} \cos(\theta) \tau_o(\lambda) \tau_w(\lambda) \tau_m(\lambda) \tau_{aa}(\lambda) \tau_R^{1.5}(\lambda) [1 - \tau_{as}(\lambda)] F_{as} \quad [3b]$$

$$I_g^{\mu}(\lambda) = \frac{I_{dir0n}(\lambda) \cos(\theta) \alpha_{sky}(\lambda) \bar{\alpha}_g^{\mu}(\lambda)}{1 - \alpha_{sky}(\lambda) \bar{\alpha}_g^{\mu}(\lambda)} \quad [3c]$$

$$I_g(\lambda) = \frac{\left[I_R(\lambda) + I_a(\lambda)\right] \alpha_{sky}(\lambda) \bar{\alpha}_g(\lambda)}{1 - \alpha_{sky}(\lambda) \bar{\alpha}_g(\lambda)} \quad [3d]$$

where θ is the solar zenith angle, F_{as} is the fraction of aerosol scatter that is directed downward, and α is the albedo. Transmittance subscripts *aa* and *as* denote aerosol absorption and aerosol scattering, respectively. Albedo subscripts *sky* and *g* denote sky reflectivity and ground reflectivity, respectively. The overbar indicates that an areal average albedo value needs to be used. Superscript μ, representing the cosine of the solar zenith angle (horizontal terrain) or the cosine of the illumination angle (sloping terrain), is used to denote direct (beam) radiation. The factor 0.5 is based on the assumption that one-half of the Rayleigh scatter is directed downward. The factors 0.95 and 1.5 are empirical correction factors to account for the fact that Rayleigh and aerosol scattering are not entirely independent of each other. The sum of I_R, I_a, and I_g is further corrected by multiplying by $(\lambda + 0.55)^{1.8}$ for $\lambda \leq 0.45$ μm (for further details, see Bird and Riordan, 1986). Additional information on the calculation of spectral atmospheric transmittances can be found in Dozier (1980) and Muneer (1997). All-sky direct irradiance on a horizontal ground surface I_{dir} is a function of cloud cover *c* (Munro and Young, 1982):

$$I_{dir}(\lambda) = I_{dir0n}(\lambda) \cos(\theta)(1 - c) \quad [4]$$

Similarly, diffuse irradiance from the cloudless portion of the sky on a horizontal surface I_{dif1} is

$$I_{dif1}(\lambda) = \left[I_R(\lambda) + I_a(\lambda) + I_g^{\mu}(\lambda) + I_g(\lambda)\right](\lambda + 0.55)^{1.8}(1 - c) \quad \lambda \leq 0.45\ \mu m \quad [5a]$$

$$I_{dif1}(\lambda) = \left[I_R(\lambda) + I_a(\lambda) + I_g^{\mu}(\lambda) + I_g(\lambda)\right](1 - c) \quad \lambda > 0.45\ \mu m \quad [5b]$$

Calculation of the diffuse irradiance from the cloudy portion of the sky I_{dif2} is complicated and the subject of ongoing research. Our method (horizontal surface) is a rough approximation based on the work of Munro and Young (1982):

$$I_{dif2}(\lambda) = c I_0(\lambda) d_{es} \cos(\theta) \tau_o(\lambda) \tau_m(\lambda) \tau_R(\lambda) \tau_a(\lambda) \max(1 - \alpha_{ct} - \beta_{cl}, 0) \quad [6]$$

where the cloud-top albedo α_{ct} is calculated through a modified expression developed by Fritz (1954) for clouds with large drops (Munro and Young, 1982). The factor β_{cl} denotes the dimensionless absorptivity of clouds. We adopted $\beta_{cl} = 0.2$ based on evidence presented by Ackerman et al. (2003). Note that the transmittance term for water vapor absorption, $\tau_w(\lambda)$, is not included in Eq. [6]. Stephens (1996) noted that cloud absorption occurs in place of, rather than in addition to, clear-sky water vapor absorption. The spectral effects of clouds on solar irradiance are not well understood (Bartlett et al., 1998), hence α_{ct} and β_{cl} are assumed to be independent of wavelength.

Additional diffuse irradiance is due to multiple scattering between the cloud base and the ground. For a horizontal surface,

$$I_{dif3}^{\mu}(\lambda) = \frac{c I_{dir}(\lambda) \alpha_{cb} \bar{\alpha}_g^{\mu}(\lambda)}{1 - \alpha_{cb} \bar{\alpha}_g^{\mu}(\lambda)} \quad [7a]$$

$$I_{dif3}(\lambda) = \frac{c\left[I_{dif1}(\lambda) + I_{dif2}(\lambda)\right] \alpha_{cb} \bar{\alpha}_g(\lambda)}{1 - \alpha_{cb} \bar{\alpha}_g(\lambda)} \quad [7b]$$

where α_{cb} is the cloud-base albedo, which is assumed to be independent of wavelength. Davies et al. (1975) reported α_{cb} values ranging from 0.2 for cirrus clouds to 0.66 for nimbostratus clouds. Following Munro and Young (1982), a constant α_{cb} value of 0.6 was selected. The total all-sky diffuse irradiance on a horizontal surface I_{dif} is now

$$I_{dif}(\lambda) = I_{dif1}(\lambda) + I_{dif2}(\lambda) + I_{dif3}^{\mu}(\lambda) + I_{dif3}(\lambda) \quad [8]$$

Terrain slope and aspect may have a significant impact on the actual irradiance received by a surface. All-sky direct irradiance on a sloping plane can be calculated by considering the incidence angle *Z*, which is the angle between the surface normal and the direction of the sun (Muneer, 1997):

$$I_{diri}(\lambda) = I_{dir0n}(\lambda) \cos(Z)(1 - c) \quad [9]$$

The simplest model for calculating diffuse irradiance on a sloping plane assumes an isotropic sky, resulting in a correction factor of $\cos^2(i/2)$, where *i* is the slope angle of the surface plane. Diffuse irradiation is not isotropic in nature, however, and is also a function of the solar zenith angle and the aspect of the slope. Hay (1979) developed a relatively simple model that differentiates between circumsolar and uniform background sky-diffuse components. For all-sky conditions, Hay's model can be written as (Muneer, 1997)

$$I_{difi}(\lambda) = I_{dif}(\lambda) \left\{ \frac{\tau_{dir}(\lambda)(1 - c)\cos(Z)}{\cos(\theta)} + \left[1 - \tau_{dir}(\lambda)(1 - c)\right] \cos^2\left(\frac{i}{2}\right) \right\} \quad [10]$$

where τ_{dir} is the direct irradiance transmittance of the atmosphere ($=\tau_o \tau_w \tau_m \tau_R \tau_a$). This equation predicts relatively high circumsolar irradiance for clear-sky conditions, and relatively high sky-diffuse irradiance for overcast sky conditions. Horizon brightening is not included in this model. Summation of the spectral irradiance estimates for the visible (<0.7 μm) and near-infrared (≥0.7 μm) wavebands completes the incoming direct and diffuse shortwave radiation calculation. The ground surface albedo for soil without

snow is estimated following Dickinson et al. (1993) and Bonan (1996) from soil color class, topsoil water content, and wavelength. The ground surface albedo for snow-covered surfaces is estimated following Marshall (1989) and Bonan (1996) as a function of snow soot content, snow grain radius, wavelength, and illumination angle. Snow albedo decreases as the illumination angle decreases, the soot content increases, and the snow grain diameter increases (Bonan, 1996). Incoming longwave radiation from the sky is calculated as

$$L_{\text{sky}} = \varepsilon_a \sigma \left(T_a + 273.15\right)^4 \cos^2\left(\frac{i}{2}\right) \quad [11]$$

where σ is the Stefan–Boltzmann constant and ε_a is the emissivity of the atmosphere. The emissivity is calculated as (Brutsaert, 1975; Kustas et al., 1994)

$$\varepsilon_a = 1.72\left(\frac{e_a}{T_a + 273.15}\right)^{1/7}\left(1 + 0.2c^2\right) \quad [12]$$

where e_a is the vapor pressure in the atmosphere (in kPa). Brutsaert's emissivity calculation assumes a standard atmosphere, which is incorrect for higher elevations where the air is relatively thin. We adopted the correction scheme of Marks and Dozier (1979) to estimate an effective emissivity that is realistic for mountainous areas.

Parameterization of Vegetation

Vegetation is characterized by specifying the vegetation height z_v, the leaf area index (LAI), stem area index (SAI), and soil cover, SC. The exposed LAI and SAI, and the effective soil cover (SC_e), are calculated as a function of the snow height, z_{sn}:

$$\text{LAI}_e = \text{LAI}\left(1 - \frac{z_{sn}}{z_v}\right) \quad [13a]$$

$$\text{SAI}_e = \text{SAI}\left(1 - \frac{z_{sn}}{z_v}\right) \quad [13b]$$

$$\text{SC}_e = \begin{Bmatrix} \text{SC} & z_{sn} < z_v \\ 0 & z_{sn} \geq z_v \end{Bmatrix} \quad [13c]$$

The interception rate by vegetation, q_{int}, does not distinguish between liquid and solid phases (Oleson et al., 2004):

$$q_{\text{int}} = \left(p_r + p_{sn}\right)\left\{1 - \exp\left[-0.5\left(\text{LAI}_e + \text{SAI}_e\right)\right]\right\} \quad [14]$$

The maximum amount of water that the canopy can hold, $W_{\max}$, (in m) is estimated as (Dickinson et al., 1993)

$$W_{\max} = 1 \times 10^{-4}\left(\text{LAI}_e + \text{SAI}_e\right) \quad [15]$$

The wetted fraction of the canopy (stems plus leaves), F_{wet}, is estimated as (Deardorff, 1978; Dickinson et al., 1993)

$$F_{\text{wet}} = \left(\frac{W}{W_{\max}}\right)^{2/3} \leq 1 \quad [16]$$

where W is the amount of intercepted water stored on the canopy. The factors 0.5 (Eq. [14]), 1×10^{-4} m (Eq. [15]), and 2/3 (Eq. [16]) are default empirical values that can be optimized if detailed interception data are available.

Canopy Energy Balance

The canopy is assumed to have zero heat capacity. It is also assumed that photosynthetic and respiratory energy transformations can be neglected. This results in the following canopy energy balance equation (Oleson et al., 2004):

$$I_{\text{nc}} + L_{\text{nc}}\left(T_c\right) - H_c\left(T_c\right) - Q_{\text{td}}\left(T_c\right) - Q_{\text{tw}}\left(T_c\right) = 0 \quad [17]$$

where I_{nc} is the solar radiation absorbed by the vegetation, L_{nc} is the longwave radiation absorbed by the vegetation, H_c is the sensible heat flux from the vegetation, Q_{td} is the latent heat flux from the dry fraction of the canopy (transpiration), and Q_{tw} is the latent heat flux from the wet fraction of the canopy (evaporation of intercepted water). All the energy fluxes except I_{nc} are a function of the canopy temperature, T_c. The energy balance is solved by finding the correct value for T_c using Newton–Raphson iteration. The expressions used for the individual energy balance terms in Eq. [17] are listed in Appendix A.

The above canopy energy balance calculation uses the surface temperature and the soil moisture status from the previous time step. This simplification reduces the computational burden because it eliminates the need for an iterative solution between the canopy energy balance, the surface energy balance, and the belowground water flow and heat transport calculations. The associated error in the overall energy balance can be minimized by selecting small time steps.

Surface Energy Balance

The ground surface can be either soil or snow. Fresh snow is incorporated at the beginning of the time step. The surface energy balance for each time step is written as

$$Q_g\left(T_g\right) = Q_r + I_{\text{ng}} + L_{\text{ng}}\left(T_g\right) - H_g\left(T_g\right) - Q_e \quad [18]$$

where Q_g is the conductive heat flux between the soil or snow subsurface and the surface as calculated by Fourier's equation, Q_r is the advected heat from rainfall, I_{ng} is the net incoming shortwave radiation, L_{ng} is the net incoming longwave radiation, H_g is the outgoing sensible heat flux, and Q_e is the outgoing latent heat flux due to evaporation and condensation. The equations used for the individual energy balance terms in Eq. [18] are given in Appendix B.

The surface energy balance is solved by calculating the surface temperature T_g using Newton–Raphson iteration. The conductive heat flux Q_g is calculated using near-surface soil or snow temperatures from the previous time step. In addition, the surface vapor pressure that is used to calculate the latent heat flux Q_e for soil surfaces without snow is obtained using the near-surface soil water pressure head and the near-surface soil temperature from the previous time step. This simplification reduces the computational burden in a similar way as for the canopy energy balance.

Snow Water Flow and Snow Physical Properties

Snow is described using a multilayer approach to allow simulation of the often nonlinear temperature profile in this medium. Thin snow layers that drop below a preset minimum thickness are

merged with an underlying layer (overlying layer in case of the bottom snow layer). Snow layers that exceed a preset maximum thickness are split into equal parts. Snow water flow and storage are calculated using

$$\frac{\partial \theta_w}{\partial t} = \frac{\partial q}{\partial z} \quad [19]$$

where θ_w is the volumetric (liquid) water content, t is time, q is the vertical water flux, and z is the vertical coordinate. The water flux in snow is assumed to be driven by gravity only and is estimated as (Colbeck and Davidson, 1973)

$$q = K_{s,sn}\left(\frac{\theta_w - \theta_r}{1 - \theta_i - \theta_r}\right)^3 \quad [20]$$

where $K_{s,sn}$ is the saturated hydraulic conductivity of the snow, θ_i is the volumetric ice content, and θ_r is the residual water content. Equations [19] and [20] are solved sequentially using the old θ_w to calculate q (Eq. [20]), which is then used to update θ_w (Eq. [19]). For snow, the residual water content is calculated as (Tarboton and Luce, 1996)

$$\theta_r = F_c \frac{\rho_{sn}}{\rho_w} \quad [21]$$

where F_c is the mass of water that can be retained per mass of dry snow (= 0.02), ρ_{sn} is the density of snow, and ρ_w is the density of water. The saturated hydraulic conductivity of snow is calculated from the snow grain diameter, d_{gr}, and ρ_{sn} using (Shimizu, 1970; Male and Gray, 1981; Jordan, 1991)

$$K_{s,sn} = 0.077 \frac{\rho_w g}{\eta} d_{gr}^2 \exp\left(\frac{-7.8\rho_{sn}}{\rho_w}\right) \quad [22]$$

where η is the viscosity of water, g is the acceleration due to gravity, and 0.077 and 7.8 are dimensionless empirical parameters. The calculation of d_{gr} is based on the US. Army Corps of Engineers SNTHERM.89 model (Jordan, 1991; snow.usace.army.mil/model_info/sntherm.html [verified 22 July 2009]). Changes in snow diameter in dry snow are primarily due to upward-moving vapor flux. This process is approximated using (Jordan, 1991)

$$\frac{\partial d_{gr}}{\partial t} = \frac{5\times10^{-7}}{d_{gr}} D_e \left(\frac{100}{P_a}\right)\left(\frac{T + 273.15}{273.15}\right)^6 \rho_T \frac{\partial T}{\partial z} \quad [23]$$

where D_e is the effective diffusion coefficient for water vapor in snow at 100 kPa and 0°C (0.92×10^{-4} m^2 s^{-1}), P_a is the atmospheric pressure (in kPa), and ρ_T is the variation of saturation vapor density with temperature. The units for the factors 5×10^{-7} and 100 are m^4 kg^{-1} and kPa, respectively. There is a marked increase in grain growth for wet snow (Colbeck, 1982). Jordan (1991) approximated this process as

$$\frac{d(d_{gr})}{dt} = \begin{cases} \frac{4\times10^{-12}}{d_{gr}}(\theta_w + 0.05) & 0 < \theta_w < 0.09 \\ \frac{4\times10^{-12}}{d_{gr}}(0.14) & \theta_w \geq 0.09 \end{cases} \quad [24]$$

where the unit for the factor 4×10^{-12} is m^2 s^{-1}. The snow compaction rate, CR, for each layer is calculated using (Jordan, 1991)

$$CR = c_1 c_2 c_3 \exp\left[-c_4(0 - T)\right] + \frac{O_{sn}}{\eta_0}\exp\left[-c_5(0 - T)\right]\exp\left(-c_6\rho_{sn}\right) \quad [25]$$

where O_{sn} is the snow overburden (kg m^{-2}) and η_0 (= 0.9×10^6 kg s m^{-2}) is a viscosity coefficient. The first part on the right side of the equation describes compaction due to snow metamorphism, while the second part describes compaction due to overburden. Recommended values for the constants are: c_1 = 2.778×10^{-6} s^{-1}, c_4 = 0.04 °C^{-1}, c_5 = 0.08 °C^{-1}, and c_6 = 0.023 m^3 kg^{-1}. The dimensionless factors c_2 and c_3 are

$$c_2 = \begin{cases} \exp\left[-0.046(\rho_{sn} - 100)\right] & \rho_{sn} > 100 \text{ kg m}^{-3} \\ 1 & \rho_{sn} \leq 100 \text{ kg m}^{-3} \end{cases} \quad [26a]$$

$$c_3 = \begin{cases} 2 & \theta_w > 0 \\ 1 & \theta_w = 0 \end{cases} \quad [26b]$$

where the factor 0.046 is in m^3 kg^{-1}. The compaction rate is used to update the thickness of each snow layer d:

$$\frac{d(d)}{dt} = -d\,CR \quad [27]$$

Finally, the new snow layer thickness is used to update the (liquid) water content θ_w and ice content θ_i of each layer. This allows the new snow density to be calculated:

$$\rho_{sn} = \theta_w\rho_w + \theta_i\rho_i \quad [28]$$

where ρ_i is the density of ice.

Soil Water Flow

Vertical soil water is calculated using a noniterative solution to the Richards equation following a procedure outlined in Ross (2003). The procedure is best explained by showing the numerical discretization. The mass balance for soil layer i can be written as

$$d_i \frac{\Delta\theta_{wi}}{\Delta t} = q_{i+1}^F - q_i^F - S_i d_i \quad [29]$$

where S is a sink term to account for root water uptake. The soil water flux at a fraction F through the time step is estimated using a Taylor series expansion:

$$q_i^F = q_i^0 + F\left(\left.\frac{\partial q_i}{\partial u_i}\right|^0 \Delta u_i + \left.\frac{\partial q_i}{\partial u_{i-1}}\right|^0 \Delta u_{i-1}\right) \quad [30]$$

where F is a dimensionless weighting factor (between 0 and 1), and u is either the volumetric soil water content θ_w (unsaturated layer) or the soil water pressure head h (saturated layer). The superscript 0 denotes the beginning of the time step. The soil water flux at the beginning of the time step is calculated using the Darcy equation:

$$q_i^0 = \frac{K_i + K_{i-1}}{2}\left(\frac{h_i - h_{i-1}}{\Delta z_i} + 1\right) \quad [31]$$

where K is the soil hydraulic conductivity. The derivatives of the soil water flux at the beginning of the time step can be obtained by differentiating the Darcy equation with respect to either θ_w or h. The sink term is calculated as

$$S_i = \frac{a_i(h)}{\sum a_i(h) d_i} \frac{SC_e Q_{td}}{\rho_w \gamma_v} \quad [32]$$

where a is the dimensionless root water uptake reduction factor as a function of soil water pressure head according to Feddes et al. (1978). In Eq. [32] it is assumed that all soil layers contribute equally to root water uptake, both below the canopy and in the interspace areas. The above expressions result in a tridiagonal system of equations that can be solved for u using the Thomas algorithm (Press et al., 1992). The weighting factor F is 0.5 if the entire soil profile is unsaturated to improve accuracy. Otherwise, $F = 1$ is used to improve stability. An additional equation for pond height h_0 is included if ponding occurs on the soil surface (Ross, 2003):

$$\frac{\Delta h_0}{\Delta t} = q^F_{top} - q^F_{surf} \quad [33]$$

where q_{top} is the net incoming water flux from precipitation and surface evaporation (no snow) or snowmelt and q_{surf} is the flux at the soil surface. The surface flux is again estimated using a Taylor series expansion:

$$q^F_{surf} = q^0_{surf} + F\left(\left.\frac{\partial q_{surf}}{\partial h_0}\right|^0 \Delta h_0 + \left.\frac{\partial q_{surf}}{\partial u_N}\right|^0 \Delta u_N \right) \quad [34]$$

where N is the number of subsurface layers (soil and bedrock, numbering is from the bottom up). The surface flux at the beginning of the time step is

$$q^0_{surf} = K_N \left(\frac{h_0 - h_N}{0.5 d_N} + 1 \right) \quad [35]$$

An adjustable time step is used in the soil water flow calculation so that the maximum change in the volumetric soil water content is 0.02 and the maximum overshoot in the surface ponding layer is –0.02 m (negative ponding layer). The soil hydraulic properties are described by combining the Brooks and Corey (1964) water retention function with the Mualem (1976) hydraulic conductivity function:

$$\frac{\theta_w - \theta_r}{\phi - \theta_r} = \left(\frac{h}{h_b} \right)^{-\chi} \quad [36a]$$

$$K = K_s \left(\frac{\theta_w - \theta_r}{\phi - \theta_r} \right)^{2 + l + 2/\chi} \times 10^{-\Omega \theta_i} \quad [36b]$$

where ϕ is the effective soil porosity, h_b is the bubbling pressure head, χ is the pore-size distribution index, K_s is the saturated soil hydraulic conductivity, and l is the pore connectivity or tortuosity factor. The soil hydraulic conductivity is reduced using an impedance factor $\Omega = 15$ to account for reduced hydraulic conductivity in frozen soils (Hansson et al., 2004). Frozen soils may exhibit steep gradients in soil water pressure heads near the freezing front. Simply averaging the soil hydraulic conductivities of two neighboring cells will overestimate the soil water flow toward the front. Hence, in frozen soil regions, only the cell with the lowest conductivity is used for K in the Darcy flow calculation (Lundin, 1990).

Snow–Soil–Bedrock Heat Transport

Heat transport in the snow–soil–bedrock continuum is calculated using the following general equation describing both heat conduction and advection:

$$\frac{\partial (C_v T)}{\partial t} = \frac{\partial}{\partial z}\left(\kappa \frac{\partial T}{\partial z} \right) + C_{v,w} \frac{\partial (qT)}{\partial z} - C_{v,w} S T \quad [37]$$

where C_v is the volumetric heat capacity and κ is the thermal conductivity. The subscript w denotes liquid water. This equation is solved using an implicit backward difference scheme for maximum numerical stability (Campbell, 1985). The effect of a possible ponding layer on the vertical heat transport is ignored in the model. The heat capacity of snow, soil, and bedrock are calculated as

$$C_v = \theta_w C_{v,w} + \theta_i C_{v,i} \text{ (snow)} \quad [38a]$$

$$C_v = (1 - \phi) C_{v,so} + \theta_w C_{v,w} + \theta_i C_{v,i} \text{ (soil)} \quad [38b]$$

$$C_v = C_{v,r} \text{ (bedrock)} \quad [38c]$$

where subscripts i, so, and r indicate ice, soil solids, and rock, respectively. The small contribution of air to the volumetric heat capacity is neglected in the above equations. The calculation of thermal conductivity is less straightforward because the spatial arrangement of the different phases is important. The snow thermal conductivity is estimated from snow density using the following expression (Jordan, 1991):

$$\kappa = \kappa_a + \left(7.75 \times 10^{-5} \rho_{sn} + 1.105 \times 10^{-6} \rho_{sn}^2 \right)(\kappa_i - \kappa_a) \text{ (snow)} \quad [39]$$

where the subscript a denotes air. The factors 7.75×10^{-5} and 1.105×10^{-6} have units $m^3\ kg^{-1}$ and $m^6\ kg^{-2}$, respectively. The soil thermal conductivity calculation follows Farouki (1981) and references therein:

$$\kappa = \kappa_{dry} + F_{KN}\left(\kappa_{sat} - \kappa_{dry} \right) \text{ (soil)} \quad [40]$$

where F_{KN} is the Kersten number and the subscripts *dry* and *sat* denote dry soil and saturated soil, respectively. The Kersten number is a function of relative water saturation, with different expressions for frozen and unfrozen soils. Details on the calculation of F_{KN}, κ_{dry}, and κ_{sat} can be found in Farouki (1981), Peters-Lidard et al. (1998), and Oleson et al. (2004). The bedrock thermal conductivity is represented by a single value, based on the rock mineral composition (e.g., Clauser and Huenges, 1995):

$$\kappa = \kappa_r \text{ (bedrock)} \quad [41]$$

No advective heat transport is calculated in the bedrock ($q = 0$). Deep percolation from the bottom of the soil profile is simply removed from the model. This water loss is the result

of downward fracture flow or lateral subsurface flow across the soil–bedrock interface.

Snow and Soil Water Phase Change

Liquid water–ice phase change in a snow layer depends on the layer temperature and on the net incoming heat flux. In soil, the energy state of the liquid water also plays a role. Capillary forces and dissolved ions reduce the energy state of the soil water, resulting in below 0°C freezing temperatures. The rate of phase change is determined by the total available energy, Q_{pc}, estimated as (e.g., Oleson et al., 2004)

$$Q_{pc} = \frac{\Delta(C_v T)}{\Delta t} - C_{v,old}\frac{0 - T_{old}}{\Delta t} \quad [42]$$

where the first term to the right of the equal sign constitutes the net incoming energy and the second term constitutes the energy storage in the layer relative to the freezing point. The net incoming energy is based on end-of-time-step values, while the relative energy storage is based on start-of-time-step values (subscript *old*). For snow, the changes in ice content, water content, and temperature due to freeze–melt can be calculated using Q_{pc}, provided that enough liquid water is present to freeze ($T < 0$, $Q_{pc} < 0$) and enough ice is present to melt ($T \geq 0$, $Q_{pc} > 0$):

$$\frac{\Delta\theta_i}{\Delta t} = -\frac{Q_{pc}}{\rho_i \gamma_f} \quad [43a]$$

$$\frac{\Delta\theta_w}{\Delta t} = \frac{Q_{pc}}{\rho_w \gamma_f} \quad [43b]$$

$$\frac{\Delta T}{\Delta t} = -\frac{Q_{pc}}{C_v} \quad [43c]$$

where γ_f is the latent heat of fusion ($\sim$333.5 kJ kg^{-1}). The same equations can be used to calculate changes in ice content, water content, and temperature in the soil due to freeze–thaw, with one additional condition. Freezing in the soil can only occur when the water potential due to capillary forces and dissolved ions is higher than the equilibrium potential of liquid water in contact with ice (Spaans and Baker, 1996; Koren et al., 1999). The equilibrium potential of liquid water in contact with ice (h_{eq} in m, $T \leq 0$°C) is calculated by integrating the Clapeyron equation, assuming zero ice pressure (Fuchs et al., 1978; Spaans and Baker, 1996):

$$h_{eq} = \frac{\gamma_f \ln\left[(T + 273.15)/273.15\right]}{g} \quad [44]$$

Soil water freezing now requires that $h + h_{osm} > h_{eq}$, where h_{osm} is the osmotic head due to dissolved ions. The osmotic head is calculated as

$$h_{osm} = -\left(\frac{\phi}{\theta_w}\right)\frac{R(T + 273.15)m'}{g} \quad [45]$$

where R is the gas constant (8.3 J mol^{-1} K^{-1}) and m' is the molality (mol solute kg^{-1} water). No solute transport is incorporated in the model and a constant molality of 1.34×10^{-2} mol kg^{-1} is assumed.

Materials and Methods

Study Area

The model was applied to a northeast-facing slope in a 0.02-km^2 subcatchment of the Dry Creek Experimental Watershed near Boise, ID. The subcatchment elevation ranges from 1600 to 1645 m above mean sea level. The summers are hot and dry. Winters are cold, with a persistent snowpack from around early November through March or April. Approximately half of the average annual precipitation of 570 mm falls as snow. Soils are classified as loamy sand and sandy loam. The soils vary in thickness from a few centimeters to about 1 m and are formed from weathering of the underlying Idaho Batholith, a granitic intrusion ranging in age from 75 to 85 million yr. A network of fractures in the bedrock enables deep percolation when the soil–bedrock interface is wet (Miller et al., 2008). The vegetation consists of sagebrush (*Artemisia tridentata* Nutt.), forbs, and grasses (Williams, 2005; McNamara et al., 2005). The northeast-facing slope of the subcatchment is 30 to 50 m long, with a slope of 25 to 30%.

The monitoring program in Dry Creek began in 1999. The northeast-facing slope that was the focus of this study is equipped with a small meteorological station that measures precipitation, barometric pressure, air temperature, relative humidity, wind speed, wind direction, and incoming solar radiation. Midslope snow depth is measured hourly using a Judd ultrasonic depth sensor (Judd Communications, Salt Lake City, UT). Midslope soil water content and soil temperature are measured in two vertical profiles that are 2 m apart. The differences between the two profiles are minor and data from only one of the profiles, designated Pit 100 by McNamara et al. (2005), were used in this study. Soil water content is measured using CS615 water content reflectometers (Campbell Scientific, Logan, UT) at depths of 5, 10, 30, 60, and 100 cm. Soil temperature is measured using thermocouples at depths of 5, 15, 30, 60, and 100 cm. The water content reflectometer readings were calibrated using manual readings from co-located time domain reflectometry sensors (Chandler et al., 2004).

Twelve snow surveys were performed using a nine-point grid on the northeast-facing slope during February and March 2001 with a Mt. Rose snow tube. The snow height, total snow water equivalent, and average snow density data from the central grid point (close to the Judd depth sensor and Pit 100) were used in this study.

Modeling Setup

Two full years were simulated for which a relatively complete data set was available. The period of 25 Aug. 2000 to 24 Aug. 2001 served as the calibration period. The period of 20 Aug. 2003 to 19 Aug. 2004 served as the validation period. Both periods started in August because of the relatively well-defined conditions during this month: the end of the growing season is near, the soil water content has been depleted, and the soil temperature is near its annual maximum.

The transmittance of the atmosphere to solar radiation was calculated following Bird and Riordan (1986). The contributions of ozone and aerosols to the transmittance were functions of the user-defined ozone amount (0.003 m) and the user-defined aerosol optical depth (0.1 in summer, 0.05 in winter). A higher aerosol

optical depth was assumed in summer to account for the higher atmospheric dust concentrations during this period. The water vapor amount used to calculate the contribution of water vapor to the transmittance was estimated from the vapor pressure and the atmospheric pressure using the empirical relationship of Garrison and Adler (1990). Transmittances due to uniformly mixed gas absorption and molecular Rayleigh scattering followed Bird and Riordan (1986), with all coefficients remaining unchanged.

Meteorological input was taken from the small meteorological station at the study site. Relative humidity, air temperature, wind speed, and precipitation were specified at 15-min intervals. No observations of cloud cover were available. Instead, cloud cover was estimated using the solar radiation data. This was achieved by first identifying clear sky days and by fitting a simple power law equation of the form $I_{tot} = b_1 d_{es}(\cos\theta)^{b_2}$ to the observed total solar radiation I_{tot} during these days (Long and Ackerman, 2000). This yielded b_1 = 1093.6 J m^{-2} s^{-1} and b_2 = 1.2 for our study site. Subsequent comparison of the power law (clear sky) I_{tot} for a given daytime period to the observed I_{tot} for that period allowed us to identify cloudy (c = 1) and uncloudy (c = 0) episodes. Nighttime cloudiness was estimated by averaging the cloudiness during the final 2 h of the preceding afternoon and the first 2 h of the following morning.

The vegetation height z_v was taken to be 0.4 m, based on the average height of the sagebrush at the soil moisture sensor site. Soil cover at the site during the summer growing season was estimated at 0.55 by Williams (2005). The maximum LAI, minimum LAI, and SAI of a single average plant at the site were estimated at 2.3, 0.2, and 0.2, respectively. In principle, bare areas and vegetated areas could be treated separately by the model; however, this is probably not appropriate when the bare and vegetated sites are closely interspersed such as at our site. Instead, we chose to consider the entire site vegetated (SC = 1), with an adjusted maximum LAI, minimum LAI, and SAI of 1.265, 0.11, and 0.11, respectively (single-plant values multiplied by 0.55). The actual LAI was assumed to be a function of the depth-average soil temperature (Dickinson et al., 1993):

$$\mathrm{LAI} = \mathrm{LAI}_{min} + (\mathrm{LAI}_{max} - \mathrm{LAI}_{min})\left[1 - 0.0016\left(25 - \overline{T}_{so}\right)^2\right] \quad [46]$$

where T_{so} is the soil temperature. Plant optical properties and plant aerodynamic parameters used in the canopy energy balance calculation were represented by parameters for the "broadleaf evergreen shrub—temperate" plant functional type as given by Oleson et al. (2004). It was assumed that the entire soil profile contributed equally to the potential root water uptake. The following root water uptake reduction factors were assumed: no reduction for soil water pressure heads between –7 and –0.01 m, and linear reduction to zero uptake for pressure heads between –7 and –160 m and for pressure heads between –0.01 and 0 m.

The density of fresh snow was calculated as a function of air temperature according to the empirical relationship of Anderson (1976). The grain diameter of fresh snow was assumed to be 0.05 mm. Fresh snow on top of existing snow was incorporated into the top snow layer by averaging the properties. This procedure minimized numerical instabilities in the heat transport calculations associated with thin snow layers. Snow layers thinner than 0.05 m were merged with neighboring layers, if present. Snow layers thicker than 0.2 m were split into two equal parts. Snow albedo, according to the Marshall (1989) and Bonan (1996) equations used, was a function of snow soot concentration, among others. The increase of soot concentration s (g g^{-1}) with time after deposition t_d was approximated in this study as

$$s = \frac{t_d}{t_{d,max}}(s_{max} - s_{min}) + s_{min} \le s_{max} \quad [47]$$

where $t_{d,max}$ is taken to be 20 d, s_{min} is 3.5 × 10^{-8} g g^{-1}, and s_{max} is 1 × 10^{-6} g g^{-1} (e.g., Hansen and Nazarenko, 2004). The land surface albedo for snowpacks thinner than 0.1 m was calculated by weighting the snow albedo and the soil albedo, assuming exponential extinction of the radiation penetration of the snow (see Tarboton and Luce, 1996).

The 1.25-m-deep soil at the site was discretized into 14 layers, with thicknesses increasing from 0.025 m at the surface to 0.2 m at the soil–bedrock interface. The underlying bedrock was discretized into 11 layers, with thicknesses increasing from 0.3 m at the soil–bedrock interface to 1.4 m at the bottom of the domain. This resulted in a total subsurface thickness of 10.45 m. The relatively thick subsurface used was important to account for the dampening effect of the bedrock heat storage on the seasonal soil temperature variations. The initial soil water content and soil temperature were derived from the reflectometer data and the thermocouple data, respectively. The initial bedrock temperature was unknown. A constant temperature of 8.9°C was assumed at the bottom of the bedrock at 10.45-m depth. This temperature was calculated by averaging the mean annual air temperatures for the calibration (8.4°C) and the validation (9.3°C) periods. Initial bedrock temperatures at shallower depths were approximated by running the model twice, first with estimated initial temperatures and then with initial values derived from the final calculated bedrock temperatures from the first run.

The top boundary for the numerical soil water flow calculations was either the soil surface (no ponding) or the ponded water surface. In both cases, a flux condition was used. This flux was determined by the difference between precipitation and evaporation (no snow) or by the melt flux from the bottom snow layer. The bottom boundary for the soil water flow calculations was the soil–bedrock interface. The exact flow conditions at this interface were difficult to define. Lateral subsurface flow, downward fracture flow, and vertical porous media flow were all probable at this boundary during all or part of the year. We simply used a free-drainage boundary condition: $q = K(\theta_w)$. Note that water flow through the bedrock was not accounted for in the model. Instead, the water flux at the soil–bedrock interface was simply removed from the model and classified as deep percolation.

The top boundary for the numerical heat transport calculation was either the soil surface (no snow) or the snow surface. In both cases, a heat flux was prescribed. This heat flux was determined by the surface energy balance. The possible presence of a ponding layer was ignored in the heat transport calculations. The bottom boundary for the heat transport calculation was set at the bottom of the bedrock. Here a constant temperature of 8.9°C was prescribed. A maximum ponding layer of 2 cm was allowed at the soil surface. Buildup of water in excess of 2 cm was removed from the model and classified as surface runoff.

Model Calibration

No attempt was made to calibrate the canopy energy balance, surface energy balance, or snowpack components of the model. The canopy and surface energy balances could not be verified because of a lack of independent data for checking the model output. The snowpack calculations contain many semitheoretical parameters that could, in principle, be optimized using the snow height, snow water equivalent, and snow density data from the subcatchment. We decided against such a calibration, given the large number of snow parameters, and given the relatively crude snow physical data set available compared with the snow studies from which the default snow parameters were developed. Only detailed snow height data were available to us, supplemented with some snow water equivalent and snow density data. Snow grain size was not measured at all. Therefore, the snow height, snow water equivalent, and snow density data were only used to check the performance of the snow calculations.

Soil hydraulic parameters in the Brooks–Corey–Mualem functions were determined using data from a single multistep outflow experiment on an undisturbed soil sample and by inverse modeling using the CS615 soil water content data from the calibration period. A homogeneous soil profile was assumed. The undisturbed sample for the multistep outflow experiment was taken from the southwest-facing slope of the 0.02-km^2 subcatchment. Initial attempts to estimate all soil hydraulic parameters from the multistep outflow using inverse methods (van Dam et al., 1994; Hopmans et al., 2002) yielded unrealistic parameter estimates due to the limited pressure head range of 0 to −150 cm covered by the outflow experiment. Determining the soil hydraulic parameters by inversely modeling the calibration period using the CS615 soil water content data with the global parameter optimization software MCS (Huyer and Neumaier, 1999) also resulted in unrealistic parameter values. The failure to obtain realistic parameter values using either method was attributed to insufficient information content in the fitting data.

Instead, a three-step calibration approach was used to determine the hydraulic properties of the soil profile. First, the van Genuchten (1980) water retention function was fitted to the pressure head–soil water content data from the outflow experiment using the RETC software (van Genuchten et al., 1991) with θ_r = 0.01. The residual water content θ_r was fixed to a realistic value for relatively coarse-textured soils to mitigate the fact that the multistep outflow experiment did not cover the dry soil range. Second, the van Genuchten parameters α_{vg} and n_{vg} were used to calculate $h_b = -1/\alpha_{vg}$ and $\chi = n_{vg} - 1$ to obtain the Brooks–Corey water retention parameters. Third, the optimum K_s value was determined by inversely modeling the calibration period using the model coupled to the MCS software with $l = 1$ and $K_s \leq 320$ cm d^{-1} and with the CS615 water content data in the objective function. The upper limit of K_s of 320 cm d^{-1} was based on results from falling-head experiments on the subcatchment soils (Gribb et al., 2009). The falling-head K_s values were expected to be relatively high because, under ponded conditions, both the soil matrix and macropores contribute to flow. Surface ponding has never been observed on the northeast-facing slope, allowing us to neglect macropores in the model.

Soil heat transport parameters were not calibrated. Instead, default parameter values were taken from the literature (Clauser and Huenges, 1995; Scharli and Rybach, 2001; Oleson et al., 2004). The specific heats of air, water, ice, and rock were 1.0, 4.2, 2.1, and 0.79 J g^{-1} K^{-1}, respectively. Volumetric heat capacities for water, ice, and rock were calculated by multiplying the specific heats with the respective densities of 1, 0.92, and 2.7 g cm^{-3}. The volumetric heat capacity for air was taken as zero because of the low density of air. The thermal conductivity of air, water, ice, and rock was 0.023, 0.57, 2.29, and 3.25 J m^{-1} s^{-1} K^{-1}, respectively. The volumetric heat capacity and thermal conductivity of soil solids were calculated from sand and clay contents using empirical equations provided by Oleson et al. (2004). A sand content of 74% and a clay content of 9% were determined using the hydrometer method on soil samples from the subcatchment (Williams, 2005).

The model calibration and validation were evaluated using graphical comparisons and modeling statistics. Two generally recommended statistical model indicators were used: root mean square error (RMSE) and modeling efficiency (EF) (Loague and Green, 1991; Vanclooster et al., 2000; Fernandez et al., 2002). The RMSE statistic gives the overestimation or underestimation percentage of the predicted value compared with the mean observed value. The EF statistic indicates the degree to which the predictions give a better estimate of the observations compared with the mean of the observations (Fernandez et al., 2002). The maximum value for EF is 1. If EF is <0, the model-predicted values are worse than simply using the observed mean (Loague and Green, 1991). The RMSE and EF values were calculated for snow height (snow sensor), depthwise soil water content, and depthwise soil temperature. No modeling statistics were calculated for snow water equivalent and snow density due to the sparse data set for these parameters.

Results and Discussion

Model Calibration Results

Measured and calculated snow height, snow water equivalent, and snow density for the calibration period at the snow sensor location near Pit 100 on the northeast-facing slope are shown in Fig. 1. The modeling statistics for snow height are given in Table 1. The timing of snow accumulation and snowmelt are captured reasonably well by the model (RMSE = 19%, EF = 0.86). Sharp decreases in the sensor-measured snow height in early February and early March are underestimated by the model. The calculated meltdown of the main snowpack in March is delayed by about 7 d. Sensor-measured and manually measured snow heights can differ significantly, showing the effect of spatial variability across short distances. The snow water equivalent is overestimated by the model by as much as 60%. The calculated average snow density is accurate in February but too high in March. The sharp calculated peaks in snow density at the start of the snow season and at the end of the snow season are due to thin snow layers that rapidly ripen and melt.

Overall, the model seems to simulate the snowpack realistically, with perhaps a small underestimation of the snow ripening and snowmelt rates. A perfect match between measured and calculated physical properties is not expected for a complicated medium such as snow. This is especially true considering the fact that the effect of wind on snow transport is not considered in the model. Snow drifting across the landscape may modify the spatial

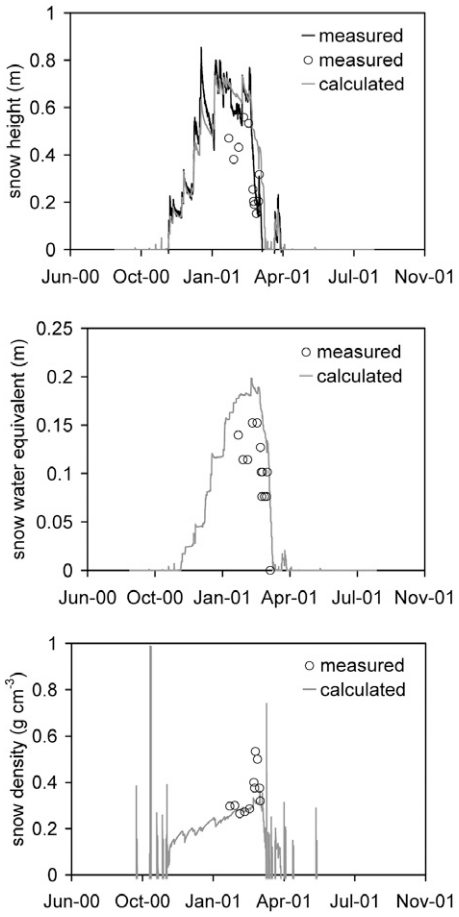

FIG. 1. Measured and calculated snow height, snow water equivalent, and snow density for the calibration period at the snow sensor location near Pit 100 on the northeast-facing slope of the subcatchment. Snow height was measured with a distance sensor (solid line) and manually (symbols). Snow water equivalent and snow density are for the entire snowpack.

TABLE 1. Model statistics for snow height, depthwise soil water content, and depthwise soil temperature for the calibration period. Both root mean square error (RMSE) and modeling efficiency (EF) are given.

Depth	Snow height		Soil water content		Soil temperature	
	RMSE	EF	RMSE	EF	RMSE	EF
cm	%		%		%	
–	19	0.86	–	–	–	–
5	–	–	22	0.84	28	0.93
30	–	–	19	0.82	13	0.97
60	–	–	18	0.83	16	0.93
100	–	–	26	0.70	14	0.93

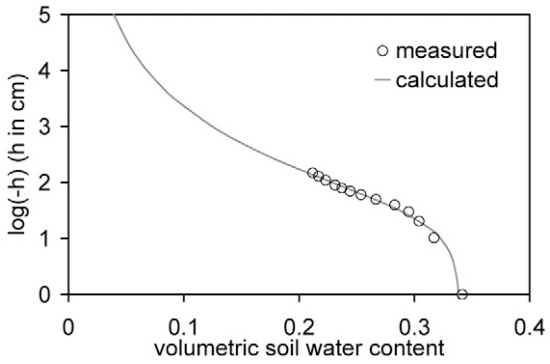

FIG. 2. Measured and calculated soil water retention. Calculated values were obtained by fitting the van Genuchten (1980) soil water retention function to retention data from a multistep outflow experiment. Optimized soil water retention parameters: saturated volumetric soil water content $\theta_s = 0.339 \sim$ porosity ϕ, van Genuchten parameters $\alpha_{vg} = 0.0344$ cm^{-1} and $n_{vg} = 1.297$. The value of the residual volumetric soil water content θ_r was not optimized but fixed to 0.01.

distribution of snow considerably, especially when vegetation is present (Essery et al., 1999; Prasad et al., 2001).

The fit between the measured (multistep outflow experiment) and calculated (RETC optimized [van Genuchten, 1980] soil water retention function) is shown in Fig. 2. The retention function with $\theta_r = 0.01$, saturated volumetric soil water content $\theta_s = 0.339$ ($\sim\phi$), $\alpha_{vg} = 0.0344$ cm^{-1}, and $n_{vg} = 1.297$ fits the data well ($R^2 = 0.991$). The values for the individual parameters seem realistic for relatively coarse-textured soils (e.g., Carsel and Parrish, 1988). Figure 2 confirms visually that the measurements are clustered in the wet soil water range, which led us to fix $\theta_r = 0.01$ in this case.

Note that we did not fit the Brooks and Corey (1964) soil water retention function directly to the data. This function is incapable of producing good fits to soil water retention data in the wet soil range because of the fact that $\theta_w = \phi$ for $h \geq h_b$. Instead, we calculated the Brooks and Corey $h_b = -1/\alpha_{vg} = -29.1$ cm and $\chi = n_{vg} - 1 = 0.297$ from the van Genuchten function. The relatively poor performance of the Brooks and Corey function in the wet range is not a major concern for the soil water flow calculations presented in this study because the soils rarely approach saturation.

The MCS-optimized value of $K_s = 38.67$ cm d^{-1} is well below the falling-head method K_s of 320 cm d^{-1}, as expected. The measured and calculated soil water content and soil temperature with depth for Pit 100 for the calibration period are shown in Fig. 3. The modeling statistics are given in Table 1. Calculated sharp decreases in the soil water content at 5-cm depth in early November and late March or early April are due to soil water freezing. The calculated ice contents, θ_i, were up to 0.19 during these periods (results not shown). In contrast, the measured soil water contents at this depth do not indicate any significant soil water freezing. Note that the dielectric constant of ice of $\sim$3 is much lower than the dielectric constant of water of $\sim$80, so that any significant soil water freezing should be picked up by the CS615 sensors. The inclusion of a litter layer in the model that shields the topsoil from the atmosphere might reduce the apparent overestimation of soil water freezing (Flerchinger, 2000).

The underestimation of the calculated soil water content at depths of 30, 60, and 100 cm during the snowpack period (November–March) may be attributed to three causes. First, the underestimation of snow ripening and snowmelt mentioned above may result in an underestimation of infiltrating meltwater during the snow period, resulting in lower than expected soil water contents. Second, the assumption of a homogeneous soil profile may be too simplistic. For example, field observations have found an illuvial clay layer of variable depth at the soil–bedrock interface in the subcatchment (Williams et al., 2008). Third, the free-drainage bottom boundary condition for soil water

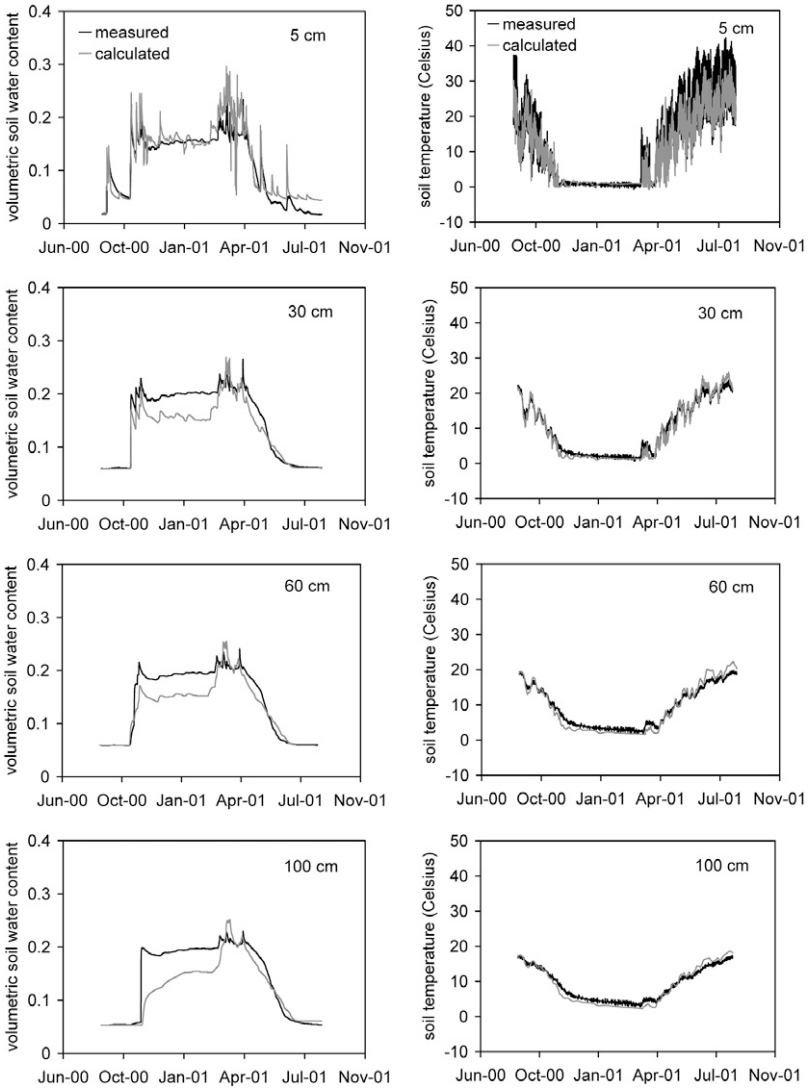

FIG. 3. Calibration period measured and calculated soil water content and soil temperature with depth for Pit 100 on the northeast-facing slope of the subcatchment.

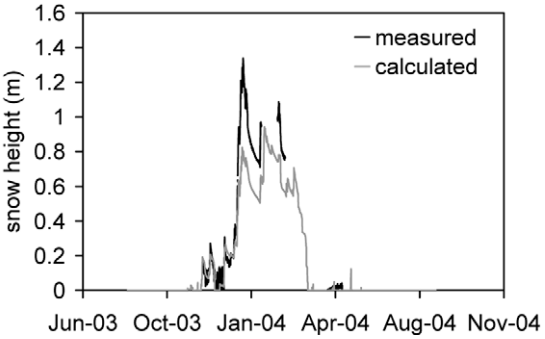

FIG. 4. Measured and calculated snow height for the validation period at the snow sensor location near Pit 100 on the northeast-facing slope of the subcatchment. Snow height was measured with a distance sensor.

flow is a gross simplification of the flow conditions at the soil–bedrock interface. Lateral inflow and outflow (e.g., McNamara et al., 2005), downward fracture flow (e.g., Miller et al., 2008), and vertical porous media flow are all possible at the interface. In fact, it is probable that the free-drainage boundary condition overestimated the downward water flow from the soil profile.

The measured and calculated soil temperatures at different depths agree well (13 < RMSE < 28%, 0.93 < EF < 0.97). The moderating effect of the snowpack from November to March on the temporal soil temperature fluctuations is clearly visible. The model underestimates the daily maximum temperature at the 5-cm depth. This may be due to the spatial discretization. The element thickness at this depth was 5 cm, while the thermocouple represents a point measurement. Note that the measured and calculated soil temperature at the 5-cm depth never falls below zero. Both the soil water freezing process during cold periods without snow, and the snowpack during periods with snow, prevent the temperature from falling below the freezing point. The good match between measured and calculated soil temperatures provides indirect evidence that the canopy and surface energy balance calculations as well as the snow and soil heat transport parameters are realistic.

Model Validation Results

The measured and calculated snow heights for the validation period at the snow sensor location near Pit 100 are shown in Fig. 4. The modeling statistics for snow height are given in Table 2. Snow accumulation at the onset of winter during November and December is captured accurately by the model. The midwinter (January) snow height is underestimated by about 25 to 40%. Unfortunately, due to equipment failure, no snow height data are available to check the calculated snow height during the melt season in March. The snowpack had completely melted by the time the equipment was back online in April.

The measured and calculated soil water content and soil temperature with depth for Pit 100 for the validation period are shown in Fig. 5. Modeling statistics are given in Table 2. No measurements are available during the first half of February and during most of March due to equipment failure. In addition, the soil water content sensor at the 30-cm depth did not function during the entire year. Note that the measured seasonal soil water content fluctuations during the validation period differ from the measured seasonal fluctuations during the calibration period. This is mainly due to significant rainfall during the second half of May. Rainfall between 10 and 28 May totaled 126 mm, far above normal values for this period.

TABLE 2. Model statistics for snow height, depthwise soil water content, and depthwise soil temperature for the validation period. Both root mean square error (RMSE) and modeling efficiency (EF) are given.No measured soil water content data at 30-cm depth were available (NA).

Depth	Snow height		Soil water content		Soil temperature	
	RMSE	EF	RMSE	EF	RMSE	EF
cm	%		%		%	
–	53	0.83	–	–	–	–
5	–	–	38	0.65	28	0.88
30	–	–	NA	NA	10	0.97
60	–	–	20	0.86	11	0.95
100	–	–	26	0.78	8	0.95

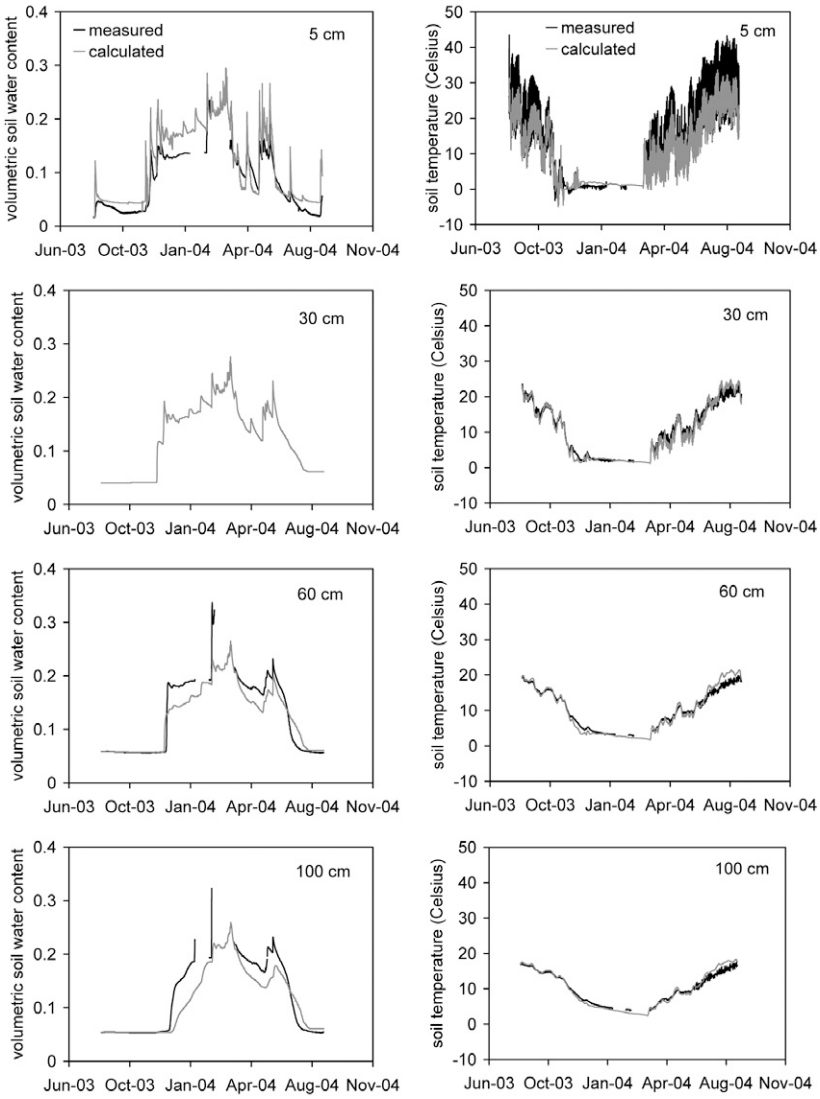

FIG. 5. Validation period measured and calculated soil water content and soil temperature with depth for Pit 100 on the northeast-facing slope of the subcatchment.

Overall, the measured and calculated soil water contents compare well (20 < RMSE < 38%, 0.65 < EF < 0.86). The soil water contents at the 5-cm depth are overestimated, while the water contents at 60- and 100-cm depths are underestimated by the model. It is especially encouraging that the May rainfall period is simulated reasonably well by the model. The surface water input is not complicated by snowmelt during this period, allowing a more straightforward evaluation of the performance of the calibrated soil hydraulic properties.

The comparison between measured and calculated soil temperature is good for all depths (8 < RMSE < 28%, 0.88 < EF < 0.97). As before, the daily maximum temperatures at 5-cm depth are underestimated by the model. Note that measured and calculated soil temperatures at the 5-cm depth fall below the freezing point for several nights during 1 to 7 November because of the lack of significant snow cover. No significant soil water freezing takes place during these nights because the soil is still dry, allowing the temperatures to drop quickly. Based on the snow height, soil water content, and soil temperature comparisons for the validation period, we conclude that the model was properly calibrated.

Water and Energy Balance

The yearly water balances for the calibration and validation periods for Pit 100 are summarized in Table 3. The table shows that yearly evapotranspiration is equivalent to 56 to 58% of the yearly precipitation. Similarly, yearly deep percolation is 39 to 43% of the yearly precipitation. Both the calibration period and the validation period show a small increase of 9 and 22 mm, respectively, in soil water storage during the year. Measured increases in soil water storage according to the CS615 sensors are only 1 and 4 mm for the calibration and validation periods, respectively (values not shown). McNamara et al. (2005) calculated the yearly water balance for Pit 100 and Pit 65 (about 2 m from Pit 100) for approximately the same period as our calibration period using the SHAW model. Their results for yearly evapotranspiration (62% of yearly precipitation) and yearly deep percolation (43% of yearly precipitation) agree with our results.

Williams (2005) used SHAW to calculate the water balance for 57 points throughout the subcatchment for a period that roughly coincides with our validation period. Averaging his results for the three points that surround Pit 100 results in yearly evapotranspiration and deep percolation values that are 68 and 37%, respectively, of yearly precipitation. Both the McNamara et al. (2005) and Williams (2005) results support the validity of our water balance calculations. It should be stressed that the deep percolation term, as used in the above discussion, is interpreted from the viewpoint of the soil profile. At the soil–bedrock interface, the downward percolation will be partitioned into lateral flow, downward fracture flow, and downward porous rock flow, depending on the exact flow conditions at the interface. Lateral unsaturated flow in moist soil above the soil–bedrock interface may also occur given the steep terrain.

The yearly energy balance for the calibration and validation periods for Pit 100 is summarized in Table 4. The calibration period shows an increase in the amount of energy stored in the soil and bedrock of 0.9 MJ m^{-2} during the calculation period, while the validation period shows a decrease of 2.7 MJ m^{-2}. These changes in energy storage are small relative to the total energy stored in the soil and the bedrock (on average 254 MJ m^{-2} in

TABLE 3. Yearly water balance for the calibration and validation periods for the Pit 100 location on the northeast-facing slope of the subcatchment.

Water balance term	Calibration period	Validation period
	mm	
Precipitation	590	716
Surface runoff	0	0
Evapotranspiration	328	416
Deep percolation	253	278
Change in soil water storage	9	22

TABLE 4. Yearly energy balance for the calibration and validation periods for the Pit 100 location on the northeast-facing slope of the subcatchment.

Energy balance term	Calibration period	Validation period
	MJ m^{-2}	
Land surface (includes vegetation)	0.2	9.7
Bottom boundary (bedrock at 10.45-m depth)	−0.7	12.4
Change in soil + bedrock energy storage	0.9	−2.7

late August, data not shown). For the calibration period, the net input of energy comes from both the surface and the subsurface. In contrast, for the validation period, the net input is solely due to the surface and a relatively large amount of energy of 12.4 MJ m^{-2} yr^{-1} escapes through the bottom boundary. It is difficult to assess the significance of these results. Lack of bedrock temperature data forced us to estimate the initial bedrock temperatures, including the temperature of 8.9°C that serves as the bottom boundary condition in the heat transport calculations.

Slagstad et al. (2008) stated that the mean annual surface temperature is the main determining factor for shallow (<1000-m depth) bedrock temperatures. The differences in sign for the average bottom heat flux for the calibration period (–0.7 MJ m^{-2} yr^{-1}) and the validation period (12.4 MJ m^{-2} yr^{-1}) appear to reflect the differences in mean annual air temperatures of 8.4 and 9.3°C, respectively. Changing the initial bedrock temperatures, altering the total thickness of the modeled domain, and modifying the temperature at the bottom boundary, however, will change the energy balance terms, as shown in Table 4. Given the good match between measured and calculated soil temperatures as shown in Fig. 3 and 5, this issue is not further explored here. Possible energy input from the deeper subsurface to the shallow bedrock due to radioactive decay introduces yet another uncertainty to the energy balance calculations.

Summary and Conclusions

A one-dimensional vertical computer model was developed to quantify the water and energy balance of vegetated areas subject to snow accumulation. The model calculates solar radiation, canopy energy balance, surface energy balance, snowpack dynamics, soil water flow, and snow–soil–bedrock heat exchange, including soil water freezing. The processes are loosely coupled (solved sequentially) to limit the computational burden. Calibration is achieved by optimizing the saturated soil hydraulic conductivity. All other model parameters are based on measurements or default values taken from the literature. Validation results show that the model can successfully calculate snow height, soil water content, and soil temperature for a northeast-facing mountain slope in the Dry Creek Experimental Watershed near Boise, ID.

Water balance results for the calibration and validation periods show that yearly evapotranspiration consumes approximately 60% of the yearly precipitation on the northeast-facing slope. Yearly deep percolation from the soil profile constitutes about 40% of the yearly precipitation. These data confirm earlier results obtained with the SHAW model by McNamara et al. (2005) and Williams (2005). The partitioning of the deep percolation from the soil into lateral flow above the soil–bedrock interface and vertical downward flow into the bedrock is still unclear. This will be the topic of a future study that will quantify spatial patterns in the water flow and heat transport.

This study, for the first time, verifies modeled soil temperatures for the Dry Creek Experimental Watershed. The results are encouraging, with excellent comparisons between measured and calculated soil temperatures. The reliability of the calculated annual energy balance for the calibration and validation periods is difficult to assess because of the lack of depthwise bedrock temperature data. Future measurements of bedrock temperature with time will be helpful in assessing the depth penetration of annual temperature fluctuations that can be used to further constrain the model.

Calibration and validation of the new model is restricted to a single mountain slope in this work. The validity of the solar spectral model, the canopy energy balance, and the ground surface energy balance is only established indirectly by comparing measured and calculated soil temperatures and, to a lesser extent, by comparing measured and calculated snowmelt. A more direct assessment of the solar spectral model and the canopy and ground surface energy balances would include comparisons against measured short- and longwave radiation and measured sensible and latent heat fluxes. Such detailed data are unavailable for the Dry Creek area. The broadband solar radiation data that are available for the area were used to calculate cloud cover and could therefore not be used to independently verify the calculated incoming solar radiation. Future model applications in areas with more elaborate data sets will be useful to further verify the model calculated energy balances.

Appendix A: Canopy Energy Balance Equations

The solar energy absorbed by the vegetation has direct beam and diffuse components that are calculated separately for the visible and near-infrared wavebands (after Oleson et al., 2004):

$$I_{nc}^{\mu}(\lambda) = I_{diri}(\lambda)\left\{1 - I\uparrow^{\mu}(\lambda) - \left[1-\alpha_g(\lambda)\right]I\downarrow^{\mu}(\lambda) - \left[1-\alpha_g^{\mu}(\lambda)\right]\exp\left[-\mathrm{OD}\left(\mathrm{LAI_e}+\mathrm{SAI_e}\right)\right]\right\} \quad [A1a]$$

$$I_{nc}(\lambda) = I_{difi}(\lambda)\left\{1 - I\uparrow(\lambda) - \left[1-\alpha_g(\lambda)\right]I\downarrow(\lambda)\right\} \quad [A1b]$$

where I^{μ} and I are upward diffuse fluxes away from the vegetation per unit incident direct beam and diffuse flux, respectively, $I\downarrow^{\mu}$ and $I\downarrow$ are downward diffuse fluxes below the vegetation per unit incident direct beam and diffuse radiation, respectively, and OD is the dimensionless optical depth for direct beam radiation. The diffuse fluxes are calculated using canopy radiative transfer relationships developed by Dickinson (1983) and Sellers (1985). The optical depth calculation is based on Sellers (1985). A complete overview of the calculation procedure is given by Oleson et al. (2004). The calculation of the longwave radiation absorbed by the vegetation follows Bonan (1996):

$$L_{nc}(T_c) = \beta_c\left(L_{sky} + L_g\uparrow\right) - 2\varepsilon_c\sigma\left(T_c + 273.15\right)^4 \quad [A2]$$

where β_c is the canopy absorptivity, ε_c is the canopy emissivity, and L_g is the upward longwave radiation from the ground:

$$L_g\uparrow = \left(1-\beta_g\right)L_c\downarrow + \varepsilon_g\sigma\left(T_g + 273.15\right)^4 \quad [A3]$$

where β_g is the ground absorptivity, ε_g is the ground emissivity, T_g is the ground temperature, and $L_c\downarrow$ is the downward longwave radiation below the canopy:

$$L_c\downarrow = (1-\beta_c)L_{sky} + \varepsilon_c\sigma(T_c + 273.15)^4 \quad [A4]$$

In practice, it is often assumed that absorptivity equals emissivity (Oleson et al., 2004). For this study, we adopted $\varepsilon_g = 0.96$ (soil), $\varepsilon_g = 0.97$ (snow), and

$$\varepsilon_c = 1 - \exp\left[\frac{-(\mathrm{LAI}_e + \mathrm{SAI}_e)}{\bar{\zeta}}\right] \quad [A5]$$

where $\bar{\zeta} = 1$ is the average inverse optical depth for longwave radiation (Bonan, 1996). The sensible heat flux from the vegetation is (Dickinson et al., 1993; Bonan, 1996; Oleson et al., 2004)

$$H_c(T_c) = \rho_a c_a (T_c - T_{ca})(\mathrm{LAI}_e + \mathrm{SAI}_e)C_{leaf} \quad [A6]$$

where ρ_a is the density of air, c_a is the specific heat capacity of air, T_{ca} is the canopy-air temperature, and C_{leaf} is the leaf boundary conductance:

$$C_{leaf} = 0.01\sqrt{\frac{v_{ca}}{d_{leaf}}} \quad [A7]$$

The factor 0.01 is the turbulent transfer coefficient between the canopy surface and the canopy air (in m $s^{-0.5}$), d_{leaf} is the characteristic dimension of the leaves in the direction of wind flow, and v_{ca} is the estimated wind velocity within the foliage layer:

$$v_{ca} = v_a\sqrt{\frac{C_{DNm}}{\varphi_m}} \quad [A8]$$

where v_a is the wind velocity at the height above the soil surface at which local meteorological data are being collected, C_{DNm} is the neutral drag coefficient for momentum, and φ_m is a stability-correction factor for momentum (see Dingman, 2002, Appendix D). The canopy-air temperature is a weighted average of the air, canopy, and ground temperatures:

$$T_{ca} = \frac{\left(v_a C_{DNh}/\varphi_m\varphi_h\right)T_a + (\mathrm{LAI}_e + \mathrm{SAI}_e)C_{leaf}T_c + v_{ca}C_{gca}T_g}{\left(v_a C_{DNh}/\varphi_m\varphi_h\right) + (\mathrm{LAI}_e + \mathrm{SAI}_e)C_{leaf} + v_{ca}C_{gca}} \quad [A9]$$

where C_{DNh} is the neutral drag coefficient for sensible heat, φ_h is a stability-correction factor for sensible heat (see Dingman, 2002), and C_{gca} is a dimensionless transfer coefficient between the ground and the canopy air that is calculated by weighing the contributions of bare ground and shaded ground (Oleson et al., 2004). The latent heat flux from plant transpiration is calculated as

$$Q_{td}(T_c) = \begin{cases} (1-F_{wet})\dfrac{\gamma_v 0.622}{R_a(T_a+273.15)}[e_0(T_c) - e_{ca}]\mathrm{LAI}_e\dfrac{C_{leaf}C_{stom}}{C_{leaf}+C_{stom}} & e_0(T_c) > e_{ca} \\ 0 & e_0(T_c) \le e_{ca} \end{cases} \quad [A10]$$

where γ_v is the latent heat of vaporization (= $2.495 - 2.36 \times 10^{-3}T$ MJ kg^{-1}), R_a is the gas constant for air (= 287 J kg^{-1} K^{-1}), e_0 is the saturation vapor pressure, e_{ca} is the canopy-air vapor pressure, and C_{stom} is the stomatal conductance. The factor 0.622 is the ratio between the molecular weight of water vapor and the molecular weight of air. The canopy-air vapor pressure is a weighted average of the air, canopy, and ground vapor pressures:

$$e_{ca} = \frac{\left(v_a C_{DNv}/\varphi_m\varphi_v\right)e_a + \mathrm{LAI}_e C_{fol}e_0(T_c) + \delta\mathrm{SAI}_e C_{leaf}e_0(T_c) + v_{ca}C_{gca}F_r e_0(T_g)}{\left(v_a C_{DNv}/\varphi_m\varphi_v\right) + \mathrm{LAI}_e C_{fol} + \delta\mathrm{SAI}_e C_{leaf} + v_{ca}C_{gca}F_r} \quad [A11]$$

where C_{DNv} is the neutral drag coefficient for latent heat, φ_v is a stability-correction factor for latent heat (see Dingman, 2002), C_{fol} is the average conductance of foliage to vapor flux, δ is equal to either F_{wet} [for $e_0(T_c) \ge e_{ca}$] or 1 [for $e_0(T_c) < e_{ca}$], and F_r is equal to either $\exp[hmg/R(T + 273.15)] \le 1$ (no snow) or 1 (snow), with h being the near-surface soil water pressure head, m the molar mass of water (0.018 kg mol^{-1}), g the acceleration due to gravity (9.81 m s^{-2}), R the gas constant (8.3 J mol^{-1} K^{-1}), and T the near-surface soil temperature. The average conductance of foliage is (Dickinson et al., 1993)

$$C_{fol} = \begin{cases} \left\{1 - \left[1 - F_{wet} - \dfrac{(1-F_{wet})C_{stom}}{C_{leaf}+C_{stom}}\right]\right\}C_{leaf} & e_0(T_c) > e_{ca} \\ C_{leaf} & e_0(T_c) \le e_{ca} \end{cases} \quad [A12]$$

The stomatal conductance is calculated as a function of the photosynthetically active net solar radiation at the canopy and the ability of plant roots to extract water from the soil (e.g., Dickinson et al., 1991; Bougeault, 1991):

$$C_{stom} = \frac{\bar{a}(h)}{r_{cmin}F_I} \quad [A13]$$

where $\bar{a}$ is the profile-average dimensionless root water uptake reduction function that depends on the soil water pressure head (Feddes et al., 1978), r_{cmin} is the minimum canopy surface resistance taken as 100 s m^{-1}, and F_I gives the dependence on the visible part of the net solar radiation that is absorbed by the canopy (about 1 for overhead sun, and r_{cmax}/r_{cmin} at night, with r_{cmax} being the maximum canopy surface resistance taken as 5000 s m^{-1}):

$$F_I = \frac{1 + \left[I^{\mu}_{nc}(\mathrm{vis}) + I_{nc}(\mathrm{vis})\right]/I_{ref}}{\left[I^{\mu}_{nc}(\mathrm{vis}) + I_{nc}(\mathrm{vis})\right]/I_{ref} + r_{cmin}/r_{cmax}} \quad [A14]$$

where I_{ref} is a reference value of the photosynthetically active net solar radiation at the canopy (taken to be 30 W m^{-2}). No temperature-dependence factor was included in the calculation of C_{stom}. The latent heat flux from the wet fraction of the canopy Q_{tw} is

$$Q_{tw}(T_c) = \delta\frac{\gamma_v 0.622}{R_a(T_a+273.15)}[e_0(T_c) - e_{ca}](\mathrm{LAI}_e + \mathrm{SAI}_e)C_{leaf} \quad [A15]$$

Appendix B: Surface Energy Balance Equations

The advected heat by rain is

$$Q_r = p_r' \rho_w c_w \max(T_a, 0) \quad [B1]$$

where p_r' is the rainfall rate after canopy interception, ρ_w is the density of water, and c_w is the specific heat of water. The net incoming direct and diffuse solar radiation for a surface that is shaded by vegetation is (after Oleson et al., 2004)

$$\begin{aligned} &I_{ng}(\lambda) = \\ &I_{diri}(\lambda)\exp\left[-OD(LAI_e + SAI_e)\right]\left[1-\alpha_g^{\mu}(\lambda)\right] \\ &+\left[I_{diri}(\lambda)I{\downarrow}^{\mu}(\lambda) + I_{difi}(\lambda)I{\downarrow}(\lambda)\right]\left[1-\alpha_g(\lambda)\right] \end{aligned} \quad [B2]$$

where $I{\downarrow}^{\mu}$ and $I{\downarrow}$ are downward diffuse fluxes below the vegetation per unit incident direct beam and diffuse radiation, respectively (Dickinson, 1983; Sellers, 1985), and OD is the dimensionless optical depth for direct beam radiation (Sellers, 1985). The net incoming direct and diffuse solar radiation for a surface that is not shaded by vegetation ($\exp[-OD(LAI_e + SAI_e)] = 1$, $I{\downarrow}^{\mu} = 0$, and $I{\downarrow} = 1$) simplifies to

$$I_{ng}(\lambda) = I_{diri}(\lambda)\left[1-\alpha_g^{\mu}(\lambda)\right] + I_{difi}(\lambda)\left[1-\alpha_g(\lambda)\right] \quad [B3]$$

The net incoming longwave radiation for a surface shaded by vegetation is (Bonan, 1996)

$$L_{ng} = \beta_g L_c{\downarrow} - \varepsilon_g \sigma \left(T_g + 273.15\right)^4 \quad [B4]$$

where β_g is the ground absorptivity, ε_g is the ground emissivity, and $L_c{\downarrow}$ is the downward longwave radiation below the canopy. Similarly, for an unshaded surface we have

$$L_{ng} = \beta_g L_{sky} - \varepsilon_g \sigma \left(T_g + 273.15\right)^4 \quad [B5]$$

The outgoing sensible heat flux at the surface is

$$H_g = \begin{cases} \rho_a c_a \left(T_g - T_{ca}\right) v_{ca} C_{gca} & \text{vegetated} \\ \dfrac{\rho_a c_a \left(T_g - T_a\right) v_a C_{DNh}}{\varphi_m \varphi_h} & \text{unvegetated} \end{cases} \quad [B6]$$

where ρ_a is the density of air, c_a is the specific heat capacity of air, T_{ca} is the canopy-air temperature, v_a is the wind velocity at the height above the soil surface at which local meteorological data are being collected, v_{ca} is the estimated wind velocity within the foliage layer, C_{gca} is a dimensionless transfer coefficient between the ground and the canopy air that is calculated by weighting the contributions of bare ground and shaded ground (Oleson et al., 2004), C_{DNh} is the neutral drag coefficient for sensible heat, and φ_m and φ_h are stability-correction factors for momentum and sensible heat, respectively (see Dingman, 2002, Appendix D). The outgoing latent heat flux for a snow-covered surface is calculated as

$$Q_e = \begin{cases} \dfrac{\gamma_s 0.622}{R_a\left(T_a + 273.15\right)}\left[e_0\left(T_g\right) - e_{ca}\right] v_{ca} C_{gca} & \text{vegetated} \\ \dfrac{\gamma_s 0.622\left(e_0(T_g) - e_a\right) v_a C_{DNv}}{R_a\left(T_a + 273.15\right)\varphi_m \varphi_v} & \text{unvegetated} \end{cases} \quad [B7]$$

where γ_s is the latent heat of sublimation (2834 J g^{-1}), R_a is the gas constant for air (= 287 J kg^{-1} K^{-1}), e_0 is the saturation vapor pressure, e_{ca} is the canopy-air vapor pressure, C_{DNv} is the neutral drag coefficient for latent heat, and φ_v is a stability-correction factor for latent heat (see Dingman, 2002). The factor 0.622 is the ratio between the molecular weight of water vapor and the molecular weight of air. The outgoing latent heat flux for soil surfaces without snow is

$$Q_e = \begin{cases} \dfrac{\gamma_v 0.622}{R_a\left(T_a + 273.15\right)}\left[e_0\left(T_g\right) - e_{ca}\right] v_{ca} C_{gca} & e_0\left(T_g\right) < e_{ca} \\ \dfrac{\gamma_v 0.622}{R_a\left(T_a + 273.15\right)}\left[F_r e_0\left(T_g\right) - e_{ca}\right] v_{ca} C_{gca} & e_{ca} < F_r e_0\left(T_g\right) \quad \text{vegetated} \\ 0 & F_r e_0\left(T_g\right) \le e_{ca} \le e_0\left(T_g\right) \\ \dfrac{\gamma_v 0.622\left[e_0\left(T_g\right) - e_a\right] v_a C_{DNv}}{R_a\left(T_a + 273.15\right)\varphi_m \varphi_v} & e_0\left(T_g\right) < e_a \\ \dfrac{\gamma_v 0.622\left[F_r e_0\left(T_g\right) - e_a\right] v_a C_{DNv}}{R_a\left(T_a + 273.15\right)\varphi_m \varphi_v} & e_a < F_r e_0\left(T_g\right) \quad \text{unvegetated} \\ 0 & F_r e_0\left(T_g\right) \le e_a \le e_0\left(T_g\right) \end{cases} \quad [B8]$$

where γ_v is the latent heat of vaporization (= 2.495 – 2.36 × $10^{-3}T$ MJ kg^{-1}), F_r is the vapor pressure reduction factor (see Appendix A), and $e_0(T_g) < e_{ca}$ and $e_0(T_g) < e_a$ are the conditions for dew formation for vegetated and unvegetated soil surfaces, respectively.

Appendix C: Notation

a	root water uptake reduction function
b	coefficients in total solar radiation calculation (subscripts 1 and 2), variable units
C	conductance (subscripts fol, leaf, and stom), m s^{-1}
C	transfer coefficient (subscript gca)
C_{DN}	neutral drag coefficient (subscripts h, m, and v)
C_v	volumetric heat capacity (subscripts a, i, old, r, so, and w), J m^{-3} K^{-1}
CR	snow compaction rate, s^{-1}
c	cloud cover
c	constants in snow compaction calculation (subscripts 1, 2, 3, 4, 5, and 6), variable units
c	specific heat capacity (subscripts a and w), J kg^{-1} K^{-1}
D_e	effective diffusion coefficient for water vapor in snow, m^2 s^{-1}
d	snow or soil layer thickness, m
d_{es}	correction factor for the Earth–sun distance
d_{gr}	snow grain diameter, m
d_{leaf}	characteristic leaf dimension in the direction of wind flow, m
e	vapor pressure (subscripts 0, a, and ca), Pa
F	fraction through the time step
F_{as}	fraction of aerosol scatter that is directed downward
F_c	mass of water that is retained per mass of dry snow
F_I	factor in the stomatal conductance calculation
F_{KN}	Kersten number
F_r	fraction in canopy-air vapor pressure calculation
F_{wet}	canopy wetted fraction
g	acceleration due to gravity, m s^{-2}
H	sensible heat flux (subscripts c and g), J m^{-2} s^{-1}
h	soil water pressure head, m
h_0	surface water ponding height, m
h_b	bubbling pressure head, m
h_{eq}	equilibrium potential of liquid water in contact with ice, m
h_{osm}	osmotic head due to dissolved ions, m

I	irradiance (subscripts 0, a, dif, dif1, dif2, dif3, difi, dir, dir0n, diri, g, nc, ng, R, ref, and tot), J m^{-2} s^{-1}
$I\downarrow$,	downward and upward diffuse flux, respectively, per unit flux
i	surface plane slope angle
K	unsaturated soil hydraulic conductivity, m s^{-1}
K_s	saturated hydraulic conductivity (subscript sn), m s^{-1}
L	long-wave radiation (subscripts c, g, nc, ng, and sky), J m^{-2} s^{-1}
l	pore connectivity or tortuosity factor
LAI	leaf area index (subscripts e, max, and min)
m	molar mass of water (0.018 kg mol^{-1})
m'	molality (mol solute kg^{-1} water)
N	number of subsurface layers
n_{vg}	pore-size distribution parameter in van Genuchten soil hydraulic functions
O_{sn}	snow overburden, kg m^{-2}
OD	optical depth for direct beam radiation
P_a	atmospheric pressure, Pa
p	precipitation rate (subscripts r and sn), m s^{-1}
Q_e	latent heat flux at ground surface, J m^{-2} s^{-1}
Q_g	conductive snow or soil heat flux, J m^{-2} s^{-1}
Q_{pc}	available energy for phase change, J m^{-3} s^{-1}
Q_r	advected heat from rainfall, J m^{-2} s^{-1}
Q_t	latent heat flux at canopy (subscripts d and w), J m^{-2} s^{-1}
q	vertical water flux (subscripts surf and top), m s^{-1}
q_{int}	vegetation interception rate, m s^{-1}
R	gas constant (8.3 J mol^{-1} K^{-1})
R_a	gas constant for air, J kg^{-1} K^{-1}
r_c	canopy surface resistance (subscripts max and min), s m^{-1}
S	root water uptake sink term, s^{-1}
SAI	stem area index (subscript e)
SC	soil cover (subscript e)
s	snow soot concentration (subscripts max and min), g g^{-1}
T	temperature (subscripts a, c, ca, g, max, min, old, and so), °C
t	time, s
t_d	time after deposition (subscript max), s
u	dummy variable (variable units)
v	wind velocity (subscripts a and ca), m s^{-1}
W	intercepted water on canopy (subscript max), m
Z	direct solar radiation incidence angle
z	height (subscripts sn and v), m
α	albedo (subscripts cb, ct, g, and sky)
α_{vg}	parameter in van Genuchten soil hydraulic functions, m^{-1}
β	absorptivity (subscripts c, cl, and g)
γ	latent heat variable (subscripts f, v, and s), J kg^{-1}
δ	fraction in canopy-air vapor pressure calculation
ε	emissivity (subscripts a, c, and g)
ζ	inverse optical depth for longwave radiation
η	water viscosity, kg m^{-1} s^{-1}
η_0	viscosity coefficient in snow compaction rate calculation, kg s m^{-2}
θ	solar zenith angle
θ	volumetric content (subscripts i, r, and w)
κ	thermal conductivity (subscripts a, dry, i, r, and sat), J m^{-1} s^{-1} K^{-1}
λ	wavelength, m
μ	cosine solar zenith angle or cosine of the illumination angle
ρ	density (subscripts a, i, sn, and w), kg m^{-3}
ρ_T	variation of saturation vapor pressure with temperature, kg m^{-3} K^{-1}
σ	Stefan–Boltzmann constant (5.7 × 10^{-8} J m^{-2} s^{-1} K^{-4})
τ	transmittance of the atmosphere (subscripts a, aa, as, dir, m, o, R, and w)
ϕ	effective soil porosity
χ	pore size distribution index
φ	stability correction factor (subscripts h, m, and v)
Ω	ice impedance factor in soil hydraulic conductivity function

Acknowledgments

This study was funded in part by USDA-CSREES SRGP Award 2005-34552-15828 and the NSF-Idaho EPSCoR program and the National Science Foundation under Award no. EPS-0447689.

References

Ackerman, T.P., D.M. Flynn, and R.T. Marchand. 2003. Quantifying the magnitude of anomalous solar absorption. J. Geophys. Res. 108(D9):4273, doi:10.1029/2002JD002674.

Anderson, E.A. 1976. A point energy and mass balance model of a snow cover. Tech. Rep. NWS 19. Office of Hydrol., Natl. Weather Serv., Silver Spring, MD.

Bartlett, J.S., A.M. Ciotti, R.F. Davis, and J.J. Cullen. 1998. The spectral effects of clouds on solar irradiance. J. Geophys. Res. 103:31017–31031.

Bird, R.E., and C. Riordan. 1986. Simple solar spectral model for direct and diffuse irradiance on horizontal and tilted planes at the earth's surface for cloudless atmospheres. J. Clim. Appl. Meteorol. 25:87–97.

Bonan, G.B. 1996. A land surface model (LSM version 1.0) for ecological, hydrological, and atmospheric studies: Technical description and user's guide. Tech. Note NCAR/TN-417+STR. Natl. Ctr. for Atmos. Res., Boulder, CO.

Bougeault, P. 1991. Parameterization schemes of land-surface processes for mesoscale atmospheric models. p. 55–92. *In* T.J. Schmugge and J. Andre (ed.) Land surface evaporation: Measurement and parameterization. Springer-Verlag, New York.

Brooks, R.H., and A.T. Corey. 1964. Hydraulic properties of porous media. Hydrol. Pap. 3. Colorado State Univ., Ft Collins.

Brutsaert, W. 1975. On a derivable formula for long-wave radiation from clear skies. Water Resour. Res. 11:742–744.

Campbell, G.S. 1985. Soil physics with BASIC. Dev. Soil Sci. 14. Elsevier, Amsterdam.

Carsel, R.F., and R.S. Parrish. 1988. Developing joint probability distributions of soil water retention characteristics. Water Resour. Res. 24:755–769.

Chandler, D.G., M. Seyfried, M. Murdock, and J.P. McNamara. 2004. Field calibration of water content reflectometers. Soil Sci. Soc. Am. J. 68:1501–1507.

Clauser, C., and E. Huenges. 1995. Thermal conductivity of rocks and minerals. p. 105–126. *In* T. Ahrens (ed.) Rock physics and phase relations: A handbook of physical constants. AGU Ref. Shelf 3. Am. Geophys. Union, Washington, DC.

Colbeck, S.C. 1982. An overview of seasonal snow metamorphism. Rev. Geophys. Space Phys. 20:45–61.

Colbeck, S.C., and G. Davidson. 1973. Water percolation through homogeneous snow. p. 242–256. *In* Int. Symp. on the Role of Snow and Ice in Hydrology, Banff, AB, Canada. Sept. 1972. IAHS Publ. 107. Inst. of Hydrology, Wallingford, UK.

Davies, J.A., W. Schertzer, and M. Nunez. 1975. Estimating global solar radiation. Boundary-Layer Meteorol. 9:33–52.

Deardorff, J.W. 1978. Efficient prediction of ground surface temperature and moisture, with inclusion of a layer of vegetation. J. Geophys. Res. 83:1889–1903.

Dickinson, R.E. 1983. Land surface processes and climate: Surface albedos and energy balance. Adv. Geophys. 25:305–353.

Dickinson, R.E., A. Henderson-Sellers, and P.J. Kennedy. 1993. Biosphere–atmosphere transfer scheme (BATS) version 1e as coupled to the NCAR community climate model. Tech. Note NCAR/TN-387+STR. Natl. Ctr. for Atmos. Res., Boulder, CO.

Dickinson, R.E., A. Henderson-Sellers, C. Rosenzweig, and P.J. Sellers. 1991. Evapotranspiration models with canopy resistance for use in climate models: A review. Agric. For. Meteorol. 54:373–388.

Dingman, S.L. 2002. Physical hydrology. 2nd ed. Prentice Hall, Englewood Cliffs, NJ.

Dozier, J. 1980. A clear-sky spectral solar radiation model for snow-covered mountainous terrain. Water Resour. Res. 16:709–718.

Essery, R., L. Li, and J. Pomeroy. 1999. A distributed model of blowing snow over complex terrain. Hydrol. Processes 13:2423–2438.

Farouki, O.T. 1981. The thermal properties of soils in cold regions. Cold Reg. Sci. Technol. 5:67–75.

Feddes, R.A., P.J. Kowalik, and H. Zaradny. 1978. Simulation of field water use and crop yield. Simul. Monogr. Pudoc, Wageningen, the Netherlands.

Fernandez, J.E., C. Slawinski, F. Moreno, R.T. Walczak, and M. Vanclooster. 2002. Simulating the fate of water in a soil–crop system of a semi-arid Mediterranean area with the WAVE 2.1 and the EURO-ACCESS-II models. Agric. Water Manage. 56:113–129.

Flerchinger, G.N. 2000. The simultaneous heat and water (SHAW) model: Technical documentation. Tech. Rep. NWRC 2000–09. Northw. Watershed Res. Ctr., Boise, ID.

Flerchinger, G.N., W.P. Kustas, and M.A. Weltz. 1998. Simulating surface energy fluxes and radiometric surface temperatures for two arid vegetation communities using the SHAW model. J. Appl. Meteorol. 37:449–460.

Fritz, S. 1954. Scattering of solar energy by clouds of large drops. J. Meteorol. 11:291–300.

Fuchs, M., G.S. Campbell, and R.I. Papendick. 1978. An analysis of sensible and latent heat flow in a partially frozen unsaturated soil. Soil Sci. Soc. Am. J. 42:379–385.

Garrison, J.D., and G.P. Adler. 1990. Estimation of precipitable water over the United States for application to the division of solar radiation into its direct and diffuse components. Sol. Energy 44:225–241.

Gribb, M.M., I. Forkutsa, A. Hansen, D.G. Chandler, and J.P. McNamara. 2009. The effect of various soil hydraulic property estimates on soil moisture simulations. Vadose Zone J. 8:321–331.

Hansen, J., and L. Nazarenko. 2004. Soot climate forcing via snow and ice albedos. Proc. Natl. Acad. Sci. 101:423–428.

Hansson, K., J. Simunek, M. Mizoguchi, L.-C. Lundin, and M.Th. van Genuchten. 2004. Water flow and heat transport in frozen soil: Numerical solution and freeze-thaw applications. Vadose Zone J. 3:693–704.

Hay, J.E. 1979. Calculation of monthly mean solar radiation for horizontal and inclined surfaces. Sol. Energy 23:301–307.

Hopmans, J.W., J. Simunek, N. Romano, and W. Durner. 2002. Inverse methods. p. 963–1008. *In* J.H. Dane and G.C. Topp (ed.) Methods of soil analysis. Part 4. Physical methods. SSSA Book Ser. 5. SSSA, Madison, WI.

Huyer, W., and A. Neumaier. 1999. Global optimization by multilevel coordinate search. J. Global Optim. 14:331–355.

Jansson, P.E., and L. Karlberg. 2004. Coupled heat and mass transfer model for soil–plant–atmosphere systems. R. Inst. of Technol., Dep. of Civil and Environ. Eng., Stockholm, Sweden.

Jordan, R. 1991. A one-dimensional temperature model for a snow cover: Technical documentation for SNTHERM.89. Spec. Rep. 91-16. U.S. Army Corps of Eng., Cold Regions Res. and Eng. Lab., Hanover, NH.

Koivusalo, H., M. Heikinheimo, and T. Karvonen. 2001. Test of a simple two-layer parameterisation to simulate the energy balance and temperature of a snow pack. Theor. Appl. Climatol. 70:65–79.

Koren, V., J. Schaake, K. Mitchell, Q. Duan, F. Chen, and J.M. Baker. 1999. A parameterization of snowpack and frozen ground intended for NCEP weather and climate models. J. Geophys. Res. 104:19569–19585.

Kustas, W.P., A. Rango, and R. Uijlenhoet. 1994. A simple energy budget algorithm for the snowmelt runoff model. Water Resour. Res. 30:1515–1527.

Lehning, M., I. Volksch, D. Gustafsson, T.A. Nguyen, M. Stahli, and M. Zappa. 2006. ALPINE3D: A detailed model of mountain surface processes and its application to snow hydrology. Hydrol. Processes 20:2111–2128.

Loague, K., and R.E. Green. 1991. Statistical and graphical methods for evaluating solute transport models: Overview and application. J. Contam. Hydrol. 7:51–73.

Long, C.N., and T.P. Ackerman. 2000. Identification of clear skies from broadband pyranometer measurements and calculation of downwelling shortwave cloud effects. J. Geophys. Res. 105:15609–15626.

Lundin, L. 1990. Hydraulic properties in an operational model of frozen soil. J. Hydrol. 118:289–310.

Male, D.H., and D.M. Gray. 1981. Snowcover ablation and runoff. p. 360–436. *In* D.M. Gray and D.H. Male (ed.) Handbook of snow: Principles, processes, management and use. Pergamon Press, Oxford, UK.

Marks, D., and J. Dozier. 1979. A clear-sky longwave radiation model for remote alpine areas. Arch. Meteorol. Geophys. Bioklimatol. 27:159–187.

Marks, D., J. Kimball, D. Tingey, and T. Link. 1998. The sensitivity of snowmelt processes to climate conditions and forest cover during rain-on-snow: A case study of the 1996 Pacific Northwest flood. Hydrol. Processes 12:1569–1587.

Marshall, S.E. 1989. A physical parameterization of snow albedo for use in climate models. Coop. Thesis NCAR/CT-123. Natl. Ctr. for Atmos. Res., Boulder, CO.

McNamara, J.P., D. Chandler, M. Seyfried, and S. Achet. 2005. Soil moisture states, lateral flow, and streamflow generation in a semi-arid, snowmelt-driven catchment. Hydrol. Processes 19:4023–4038.

Miller, C.R., P.S. Routh, T.R. Brosten, and J.P. McNamara. 2008. Application of time-lapse ERT imaging to watershed characterization. Geophysics 73(3):G7–G17.

Mualem, Y. 1976. A new model for predicting the hydraulic conductivity of unsaturated porous media. Water Resour. Res. 12:513–522.

Muneer, T. 1997. Solar radiation and daylight models for energy efficient design of buildings. Architectural Press, Oxford, UK.

Munro, D.S., and G.J. Young. 1982. An operational net shortwave radiation model for glacier basins. Water Resour. Res. 18:220–230.

Niu, G., and Z. Yang. 2006. Effects of frozen soil on snowmelt runoff and soil water storage at a continental scale. J. Hydrometeorol. 7:937–952.

Oleson, K.W., Y. Dai, G. Bonan, M. Bosilovich, P. Dirmeyer, F. Hoffman, et al. 2004. Technical description of the Community Land Model (CLM). Tech. Note NCAR/TN-461+STR. Natl. Ctr. for Atmos. Res., Boulder, CO.

Oleson, K.W., G. Niu, Z. Yang, D.M. Lawrence, P.E. Thornton, P.J. Lawrence, R. Stockli, R.E. Dickinson, G.B. Bonan, S. Levis, A. Dai, and T. Qian. 2008. Improvements to the Community Land Model and their impact on the hydrological cycle. J. Geophys. Res. 113:G01021, doi:10.1029/2007JG000563.

Peters-Lidard, C.D., E. Blackburn, X. Liang, and E.F. Wood. 1998. The effect of soil thermal conductivity parameterization on surface energy fluxes and temperatures. J. Atmos. Sci. 55:1209–1224.

Prasad, R., D.G. Tarboton, G.E. Liston, C.H. Luce, and M.S. Seyfried. 2001. Testing a blowing snow model against distributed snow measurements at Upper Sheep Creek, Idaho, United States of America. Water Resour. Res. 37:1341–1356.

Press, W.H., S.A. Teukolsky, W.T. Vetterling, and B.P. Flannery. 1992. Numerical recipes in FORTRAN. 2nd ed. Cambridge Univ. Press, Cambridge, UK.

Ross, P.J. 2003. Modeling soil water and solute transport: Fast, simplified numerical solutions. Agron. J. 95:1352–1361.

Scharli, U., and L. Rybach. 2001. Determination of specific heat capacity on rock fragments. Geothermics 30:93–110.

Sellers, P.J. 1985. Canopy reflectance, photosynthesis and transpiration. Int. J. Remote Sens. 6:1335–1372.

Shimizu, H. 1970. Air permeability of deposited snow. Contrib. 1053. Inst. of Low Temperature Science, Sapporo, Japan.

Simunek, J., M.Th. van Genuchten, and M. Sejna. 2005. The Hydrus-1D software package for simulating the one-dimensional movement of wter, heat, and multiple solutes in variably-saturated media. Univ. of California, Riverside.

Slagstad, T., K. Midttome, R.K. Ramstad, and D. Slagstad. 2008. Factors influencing shallow (<1000 m depth) temperatures and their significance for extraction of ground-source heat. p. 99–109. *In* T. Skagstad (ed.) Geology for society. Spec. Publ. 11. Geol. Surv. of Norway, Trondheim.

Spaans, E.J.A., and J.M. Baker. 1996. The soil freezing characteristic: Its measurement and similarity to the soil moisture characteristic. Soil Sci. Soc. Am. J. 60:13–19.

Stephens, G.L. 1996. How much solar radiation do clouds absorb? Science 271:1131–1133.

Tarboton, D.G., and C.H. Luce. 1996. Utah energy balance snow accumulation and melt model (UEB): Computer model technical description and users guide. Utah Water Res. Lab., Logan.

U.S. Army Corps of Engineers. 1956. Snow hydrology: Summary report of the snow investigations. U.S. Army Corps of Eng., North Pacific Div., Portland, OR.

Vanclooster, M., J.J.T.I. Boesten, M. Trevisan, C.D. Brown, E. Capri, O.M. Eklo, B. Gottesburen, V. Gouy, and A.M.A. van der Linden. 2000. A European test of pesticide-leaching models: Methodology and major recommendations. Agric. Water Manage. 44:1–19.

van Dam, J.C., P. Groenendijk, R.F.A. Hendriks, and J.G. Kroes. 2008. Advances of modeling water flow in variably saturated soils with SWAP. Vadose Zone J. 7:640–653.

van Dam, J.C., J.N.M. Stricker, and P. Droogers. 1994. Inverse method to determine soil hydraulic functions from multistep outflow experiments. Soil Sci. Soc. Am. J. 58:647–652.

van Genuchten, M.Th. 1980. A closed-form equation for predicting the hydraulic conductivity of unsaturated soils. Soil Sci. Soc. Am. J. 44:892–898.

van Genuchten, M.Th., F.J. Leij, and S.R. Yates. 1991. The RETC code for quantifying the hydraulic functions of unsaturated soils. U.S. Salinity Lab., Riverside, CA.

Williams, C.J. 2005. Characterization of the spatial and temporal controls on soil moisture and streamflow generation in a semi-arid headwater catchment, Dry Creek Experimental Watershed, Boise, Idaho. Master's thesis. Boise State Univ., Boise, ID.

Williams, C.J., J.P. McNamara, and D.G. Chandler. 2008. Controls on the temporal and spatial variability of soil moisture in a mountainous landscape: The signatures of snow and complex terrain. Hydrol. Earth Syst. Sci. Discuss. 5:1927–1966.

Wiscombe, W.J., and S.G. Warren. 1980. A model for the spectral albedo of snow: I. Pure snow. J. Atmos. Sci. 37:2712–2733.